



**HAL**  
open science

## Evaluation of neutron flux and fission rate distributions inside the JSI TRIGA Mark II reactor using multiple in-core fission chambers

Tanja Goričanec, Gašper Žerovnik, Loïc Barbot, Damien Fourmentel, Christophe Destouches, Anže Jazbec, Luka Snoj

### ► To cite this version:

Tanja Goričanec, Gašper Žerovnik, Loïc Barbot, Damien Fourmentel, Christophe Destouches, et al.. Evaluation of neutron flux and fission rate distributions inside the JSI TRIGA Mark II reactor using multiple in-core fission chambers. *Annals of Nuclear Energy*, 2018, 111, pp.407-440. 10.1016/j.anucene.2017.08.017 . cea-02388660

**HAL Id: cea-02388660**

**<https://cea.hal.science/cea-02388660v1>**

Submitted on 2 Dec 2019

**HAL** is a multi-disciplinary open access archive for the deposit and dissemination of scientific research documents, whether they are published or not. The documents may come from teaching and research institutions in France or abroad, or from public or private research centers.

L'archive ouverte pluridisciplinaire **HAL**, est destinée au dépôt et à la diffusion de documents scientifiques de niveau recherche, publiés ou non, émanant des établissements d'enseignement et de recherche français ou étrangers, des laboratoires publics ou privés.

# Evaluation of neutron flux and fission rate distributions inside the JSI TRIGA Mark II reactor using multiple in-core fission chambers

Tanja Kaiba<sup>a,1,\*</sup>, Gašper Žerovnik<sup>a,2</sup>, Loïc Barbot<sup>b</sup>, Damien Fourmentel<sup>b</sup>, Christophe Destouches<sup>b</sup>, Anže Jazbec<sup>a</sup>, Luka Snoj<sup>a</sup>

<sup>a</sup>Jožef Stefan Institute, Jamova cesta 39, SI-1000 Ljubljana, Slovenia

<sup>b</sup>CEA, DEN, DER, Instrumentation, Sensors and Dosimetry Laboratory, Cadarache, F-13108 St-Paul-Lez-Durance, France

---

## Abstract

Within the bilateral project between the CEA Cadarache and the Jožef Stefan Institute (JSI) a wide variety of measurements using multiple fission chambers simultaneously inside the reactor core were performed. The fission rate axial profiles were measured at different measuring positions and at different control rod configurations. A relative comparison of calculated fission rates using the MCNP code and the measured fission rates was performed. In general the agreement between the measurements and calculations is good, with deviations within the uncertainties. For better observation and understanding of neutron flux redistributions due to the control rod movement, the neutron flux and fission rate had been tallied through the entire reactor core for different control rod configurations. The optimal detector position with minimum signal variation due to the control rod movement was determined.

*Keywords:* research reactor, TRIGA, fission chamber, MCNP, multiple in-core detectors, control rod movement, neutron flux redistribution, fission rate profile, neutron flux profile

*PACS:* 24.10.L, 28.20.-v

---

## 1. Introduction

The TRIGA Mark II reactor in Ljubljana (Snoj and Smodiš, 2011a) is a 250 kW light-water, pool type research reactor cooled by natural convection. Similarly as other research reactors (Aghara and Charlton, 2006; Jonah et al., 2006; Merz et al., 2011), its primary purpose is education and training (Snoj et al., 2011a) of students and future reactor operators. The TRIGA research reactor in Ljubljana is also used for wide variety of other activities, such as: verification and validation of nuclear data and computer codes (Snoj and Ravnik, 2008; Snoj et al., 2011b; Trkov et al., 2009) or irradiation of various samples (Kovačević et al., 2006). Due to the very well characterized neutron and gamma fields it is lately extensively used as source of neutrons and gammas for use in nuclear analytical techniques, e.g. neutron activation analysis (Radulović et al., 2013), irradiation of silicon detectors (Cindro et al., 2009; Kramberger et al., 2010), radiation damage studies of detector material and of reading electronics for the ATLAS detector in CERN (Kramberger et al., 2007a) and irradiation of SiO<sub>2</sub> nano-material for space application (Huseynov et al., 2014, 2015a,b).

This research was carried out within the collaboration between the CEA Cadarache and the Jožef Stefan Institute (JSI), to improve the accuracy of the current on-line power monitoring system at the JSI TRIGA reactor. In previous research (Kaiba et al., 2015) the evaluation of single in-core fission chamber (FC) and a search of optimal detector position in individual measuring positions

---

\*Corresponding author

*Email addresses:* [tanja.kaiba@ijs.si](mailto:tanja.kaiba@ijs.si) (Tanja Kaiba), [gasper.zerovnik@ijs.si](mailto:gasper.zerovnik@ijs.si) (Gašper Žerovnik), [loic.barbot@cea.fr](mailto:loic.barbot@cea.fr) (Loïc Barbot), [damiens.fourmentel@cea.fr](mailto:damiens.fourmentel@cea.fr) (Damien Fourmentel), [christophe.destouches@cea.fr](mailto:christophe.destouches@cea.fr) (Christophe Destouches), [anze.jazbec@ijs.si](mailto:anze.jazbec@ijs.si) (Anže Jazbec), [luka.snoj@ijs.si](mailto:luka.snoj@ijs.si) (Luka Snoj)

<sup>1</sup>Tel.: +38615885239

<sup>2</sup>Currently at Institute for Reference Materials and Measurements, EC-JRC-IRMM, Retieseweg 111, B-2440 Geel, Belgium.

were performed. In this paper the previous research was upgraded by performing measurements with multiple in-core FCs simultaneously. In small research reactors such as TRIGA, the neutron flux profile inside the reactor core changes significantly in the axial and radial direction (Chiesa et al., 2015; Lin et al., 2006; Meftah et al., 2006; Stamatelatos et al., 2007; Štancar et al., 2012, 2015; Žerovnik et al., 2015). The major effect of neutron flux redistribution is due to the control rod (CR) movement. The neutron flux redistribution affects the power readings of current ex-core power monitoring system (Štancar and Snoj, 2014). Using multiple in-core detectors gives a possibility to average out the dependence of the detector signal on the CR position (Žerovnik et al., 2014a). Measurements of full axial profiles were performed at different CR positions. This enables extraction of a broad range of useful information, from axial neutron flux profiles to evaluation of neutron flux redistribution due to the CR movement. In general measurements are in good agreement with the Monte Carlo neutron transport code MCNP calculations (Goorley et al., 2012). In further research the neutron flux and fission rate have been calculated across the entire reactor core using the MCNP code. In search for optimal detector position inside the reactor core the fluctuation of the detector signal due to CR movement, represented by the  $\chi^2$  value for the calculated neutron flux and fission rate, has been visualized.

The paper is structured as follows. In Section 2 the JSI TRIGA Mark II research reactor, computational model, fission chamber design and experimental set-up are described. In Section 3 different measurements and comparison with calculations are presented. The comparison of axial profiles at different radial positions and for different CR configurations is presented. Within this section also the comparison of the detector signal at different axial and radial positions as a function of CR configuration is shown. In Section 4 the visualization of the calculated fission rate and the neutron flux profiles with calculated  $\chi^2$  as a function of the FC position through the entire reactor core is represented.

## 2. JSI TRIGA reactor

The TRIGA Mark II reactor at the JSI is a 250 kW light-water, pool type research reactor, cooled by natural convection.

Power monitoring is performed with five independent neutron detectors covering the entire operational range from start up in mW range to pulse mode operation up to 1 GW. They are called start-up, linear, logarithmic, safety and pulse channel. Start-up channel contains fission counter, linear and logarithmic channel have compensated ionisation chambers, while safety and pulse channel contain uncompensated ionisation chamber. These detectors are located outside the reactor core and enable continuous neutron flux measurements. The ex-core detectors can be used to determine the reactor power with 2 % uncertainty (Štancar and Snoj, 2014). The detectors are placed on the bottom of aluminium tube-like instrumentation chambers, approximately from 23.3 cm to 44.4 cm above the core mid plane. The instrumentation chamber is 67.3 cm high and has an outer diameter of 11.4 cm. The reactor core configuration with ex-core detector channels is shown in Figure 1. The reactor core has a diameter of 44.2 cm and active fuel height of 38.1 cm. There are 91 positions inside the reactor core available for positioning of fuel elements, control rods, irradiation channels, etc. and are shown in Figure 1. FCs can be located in the additional 26 holes in the metal grid above the reactor core. These measuring positions (MP) enable measurements of neutron flux in any axial position and have different diameters (10 mm and 8 mm).

There are 4 CRs inside the reactor core. In normal operation only regulating (R) and compensating (C) CRs are partially inserted and pulse (P) and safety (S) CRs are fully withdrawn at all times. R, C and S CRs consist of two parts. The lower part contains fuel, while the upper part contains strong neutron absorber  $B_4C$ . When CRs are inserted, the upper part with neutron absorber is inside at the active fuel height and the opposite when rod is withdrawn. Pulse CR features an air follower instead of fuel in the lower part.

### 2.1. Computational model

Calculations were performed with the Monte Carlo neutron transport code MCNP6 (Goorley et al., 2012) and the nuclear data library used in the calculations was ENDF/B-VII.1 (Chadwick et al., 2011). A full 3D JSI TRIGA reactor model used in calculations is based on the criticality benchmark model (Jeraj and Ravnik, 1999) which is thoroughly described in the International Handbook of

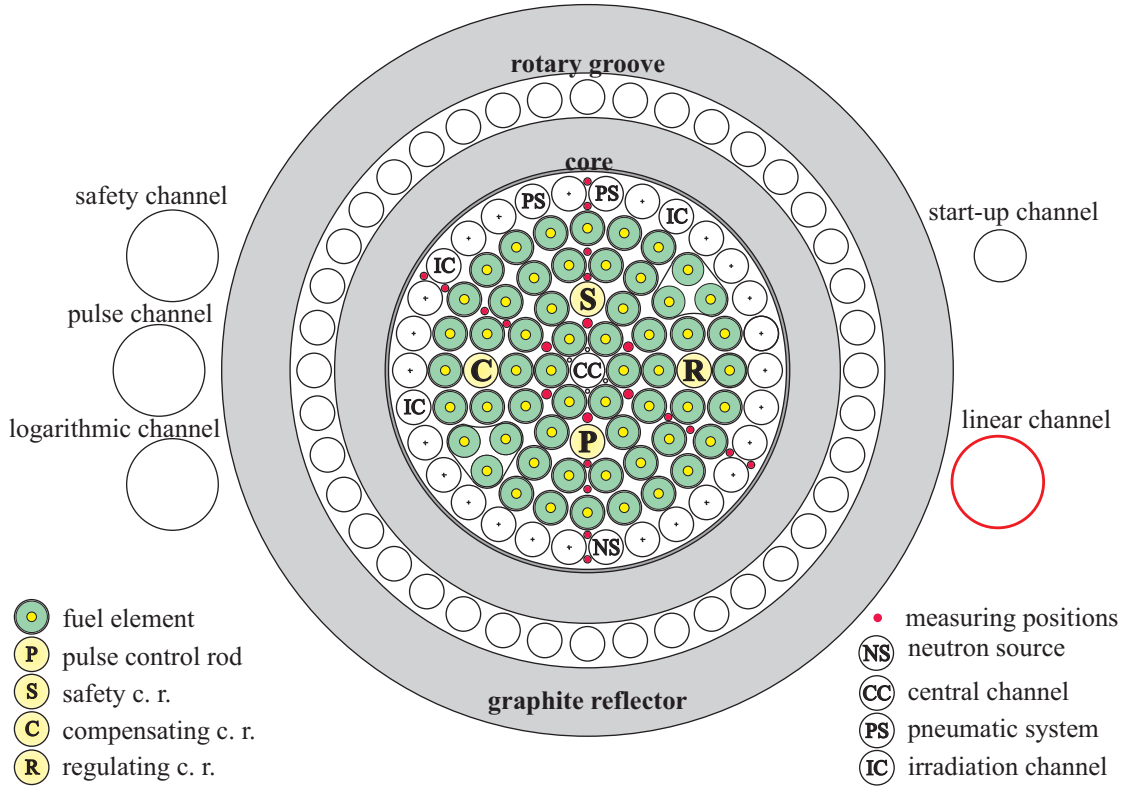


Figure 1: Reactor core configuration with current neutron detector locations: safety, pulse, logarithmic, start-up and linear channel. Control rods are denoted as safety (S), pulse (P), compensating (C) and regulating (R). Measuring positions inside reactor core are presented with red dots.

Evaluated Criticality Safety Benchmark Experiments (ICSBE, 2009). Our computational model has been expanded, verified and validated by many experiments for different calculations: the effective multiplication factor  $k_{eff}$  (Ravnik and Jeraj, 2003), power peaking factors (Snoj and Ravnik, 2008), reactor kinetic parameters (Snoj et al., 2010), flux and reaction rate distributions (Snoj et al., 2011b), neutron spectra and other reactor parameter calculations.

For calculations used in this paper, the meshtally option in MCNP was used to determine the reaction rate distributions in measuring positions and through the reactor core. For this purpose two types of meshes were made. For analysing detector response in individual MP a mesh of 210 cylindrical cells with 0.2 cm in radius and 0.4 cm in height, in which the fission density (reaction rate) was calculated, was superimposed over the reactor core (and placed above/below reactor core). Second type of mesh consisted of  $250 \times 250 \times 50$  cells in Cartesian geometry with single cell dimension of  $0.18 \text{ cm} \times 0.18 \text{ cm} \times 1.4 \text{ cm}$ . Second mesh covered the entire reactor core, which enabled comparison of reaction rate redistribution due to the CR movements in entire reactor core planes at different axial positions.

Due to the relatively low burnup and measurements performed at low powers ( $\sim 100 \text{ W}$ ), the reactor fuel was modelled as fresh at room temperature. In the JSI TRIGA reactor MCNP model Al guide tubes were added in the FCs measuring positions, however FCs were not modelled inside them, which is justified by the relative evaluation of measurements. Guide tubes were modelled as 249 cm long cylinders, beginning from the upper surface of the water tank. The impact of Al guide tubes on  $k_{eff}$  was evaluated to be negligible.

For normalizing results for fission rate and neutron flux obtained with the MCNP to absolute values the normalization factor would have to be used (Žerovnik et al., 2014b):

$$k = \frac{P\nu}{w_f k_{eff}}, \quad (1)$$

where  $P$  represents reactor power,  $k_{eff}$  is calculated effective multiplication factor,  $\nu$  represents

calculated average number of neutrons produced per fission and  $w_f$  is average energy released per fission. The  $\nu$  and  $w_f$  are constants for individual core configuration and were calculated using MONACO to be:  $\nu = 2.439$  and  $w_f = 193.7$  MeV.

## 2.2. CEA designed fission chambers

The CEA manufactured FCs with integrated mineral cable are presented in Figure 2, they have approximately 4 mm sensitive length and 3 mm in diameter.

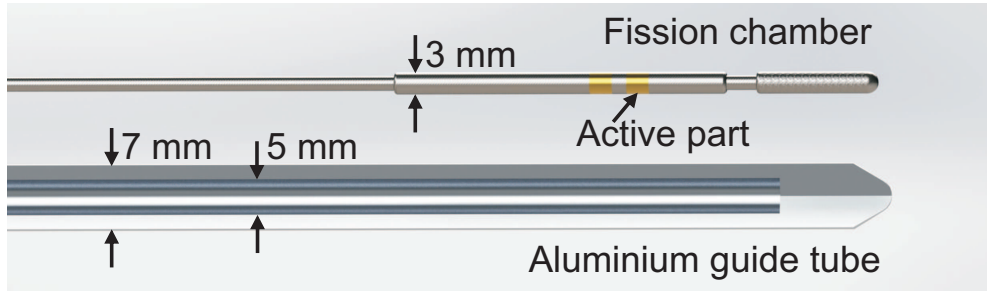
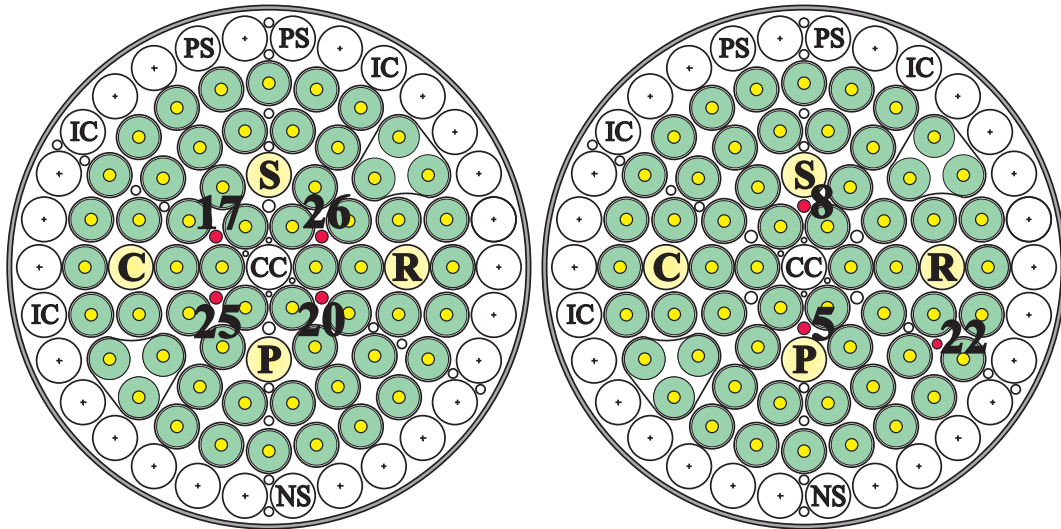


Figure 2: Schematic view of a PHOTONIC PR fission chamber assembled at CEA Cadarache. On the lower part of the figure schematic view of aluminium guide tube is presented.

Three FCs contained approximately  $10 \mu\text{g}$  of 97.663 % enriched  $^{235}\text{U}$  and one FC (in MP17) had  $10 \mu\text{g}$  of 98.49 % enriched  $^{235}\text{U}$  (Geslot et al., 2009). FC were all tested and calibrated in the CEA Cadarache facilities. For performing and analysing the measurements CEA design MONACO (Multichannel Online Neutron Acquisition in Campbell mOde) system (Thevenin et al., 2014) was used.

Measurements analysed in this paper were performed in two experimental sets. In the first experimental set 4 FC were located in MP20, MP26, MP25 and MP17 (see Figure 3a) inside the reactor core at same axial positions.



(a) First experimental set with fission chambers in measuring positions 20, 26, 25 and 17. (b) Second experimental set with fission chambers in measuring positions 8, 5 and 22.

Figure 3: Chosen measuring positions for both experimental sets.

All FCs were located inside the Al guide tubes and were moving vertically through the reactor. Within the second experimental set 3 in-core FCs were located inside MP5, MP8 and MP22 (see

Figure 3b). All 3 FCs were located inside the aluminium guide tubes. Contrary to the experiments performed in the first set, within the second set of experiments the FC located in MP22 was at a constant axial position approximately in the middle of the active fuel height and served as a reference counter. Measurements in both sets were performed in different axial positions and at different CR configurations.

### 2.3. Experimental setup

During the experiment FCs were inserted inside the aluminium guide tube as seen in Figure 4a, which were inserted inside the reactor core in before mentioned measuring positions. Those measuring positions were chosen due to their symmetric position inside the reactor core and the symmetric positions regarding to the R and C CRs. Positions of FCs were changed manually in steps of 5 cm. During the experiment all FCs were always at the same axial position inside the reactor core, estimated uncertainty in the axial position being  $\pm 1$  mm. The only exception was the FC located inside MP22, which was at constant axial position ( $(475.3 \pm 2)$  mm from the bottom of Al guide tube) during whole second experimental set.

The schematic view of fuel and CRs configuration inside the core is presented in Figure 4b, where on top in gray is the upper grid, where the reference point for measurements and calculations was chosen. Due to the reference point above the reactor core, axial positions are reported with a negative sign, where -324 mm represents the middle of the active fuel part. Comparison of the measurements with the calculations was mostly performed in 3 axial positions marked in Figure 4b with a dashed line. We must take into account that the reactor was critical during the measurements with constant power, therefore when R CR was withdrawn, the reactivity was compensated by the insertion of C CR.

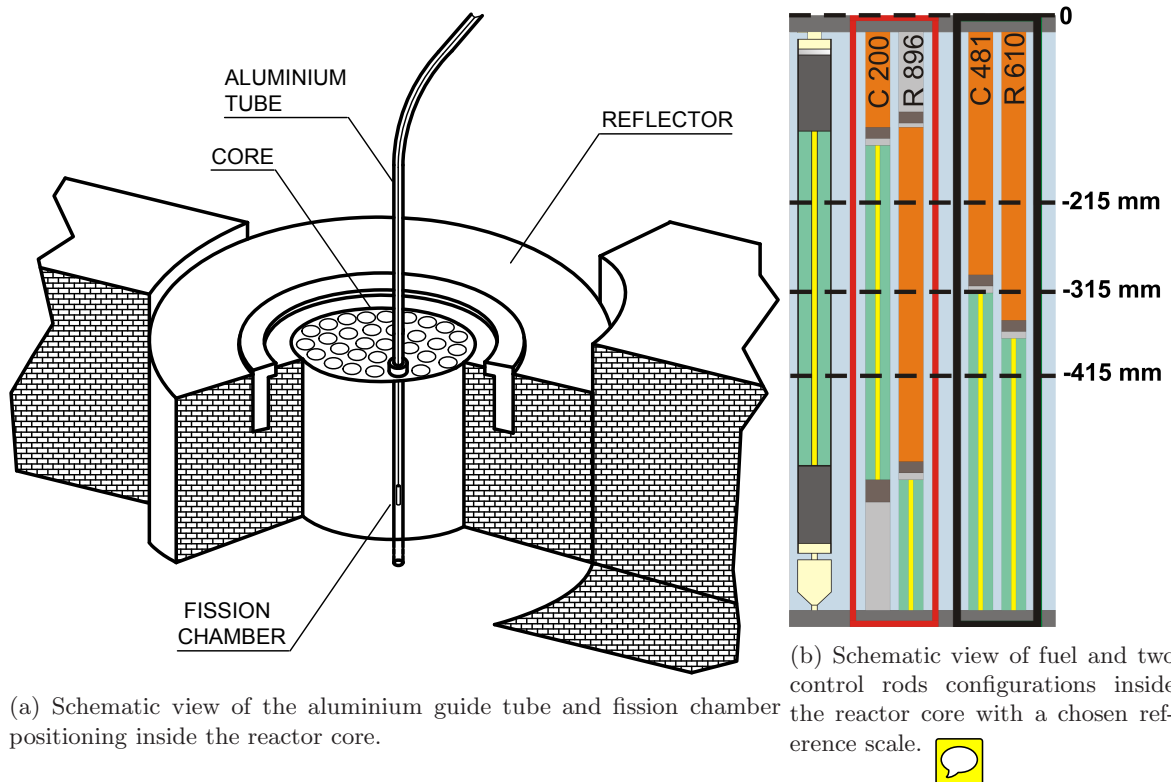



Figure 4: Schematic views of experimental configuration.

The important difference between both experimental sets is in the way aluminium guide tube was positioned inside the reactor. In most MPs aluminium guide tube can pierce through the lower reactor grid and is fixed when it sits on the top of the upper grid. In this case the FC position inside the

reactor core is determined by the dimensions of aluminium guide tube. In some MPs there is no hole inside the bottom grid (e.g. MP5 and MP8), in those MPs guide tube is not completely fixed and has bigger uncertainty in position and consequently also FC has bigger uncertainty in position 

### 3. Results

During the experiment the reactor was at constant power with minimal deviations from the reference power level, which are included in the measurement uncertainties. Therefore a relative comparison without additional normalization could be performed.

Two experimental sets were performed at different CR configurations as presented in Tables 1 and 2. During the individual measurement CRs position changed for a few steps, because FCs were moving through the reactor core while reactor power was kept constant. CRs steps near the fully withdrawn (200) or fully inserted (900) position have smaller values (reactivity) and small deviations between calculation and experimental positions are not significant.

Table 1: Regulating (R) and compensating (C) control rod positions for the first experimental set. Experimental (exp) and calculation (cal) positions are reported.

Exp. No.	$R_{exp}$ [step]	$C_{exp}$ [step]	$R_{cal}$ [step]	$C_{cal}$ [step]
1	896	200	896	200
2	740-754	349	747	349
3	615-605	481	610	481
4	500-508	582	504	582
5	380-369	705	380	704
6	220	836	220	845

Table 2: Regulating (R) and compensating (C) control rod positions for the second experimental set. Experimental (exp) and calculation (cal) positions are reported.

Exp. No.	$R_{exp}$ [step]	$C_{exp}$ [step]	$R_{cal}$ [step]	$C_{cal}$ [step]
1	900	222-244	900	233
2	740-733	366	737	366
3	615-621	480	618	480
4	499-494	594	497	594
5	380-386	703	383	703
6	241-224	854	242	854

#### 3.1. First experimental set

In the first experimental set 4 FCs were placed simultaneously inside the reactor core in MP20, MP26, MP25 and MP17 (see in Figure 3a). Experimental and calculational CR positions are reported in Table 1.

##### 3.1.1. Axial profiles

Fission rate axial profiles were measured at the above mentioned MPs at different CR configurations presented in Table 1, which enabled a broad range of possible comparisons, e.g. axial profiles at different CR configurations or deviations in detector signal at fixed axial position due to the control rod movement. All measured axial profiles are presented in Appendix A.

Calculated and measured FC axial profiles were evaluated relatively, i.e. only the shape of the fission rate profile was compared, which was achieved by normalization to the surface area below the graph. Surface area was calculated using the trapezoidal method:

$$S(z_i) = \frac{I_i}{I_0}, \quad I_0 = \frac{1}{2} \sum_{i=1}^U (I_{i+1} + I_i)(z_{i+1} - z_i), \quad (2)$$

where:

- $z_i$  ... axial position of  $i^{th}$  measurement or calculation,
- $I_i$  ... measured or calculated value at axial position  $z_i$ ,
- $I_0$  ... normalization factor,
- $S(z_i)$  ... normalized value of  $i^{th}$  measurement or calculation,
- $U$  ... number of measurements or calculations.

The comparison of the measured and calculated fission rate axial profiles is shown in Figures 5 and 6 at two different CR configurations. The difference in the axial profiles in the same MP at different CR configurations can be observed. The configuration of control rods and their position inside the reactor core are presented in Figure 4b. The effects of CR movement are also consequence of the different CR configuration. From Figures 5 and 6 can be concluded that with withdrawal of R CR, the maximum of the axial profile shifts to the lower axial position. Since the CRs consist of two parts: top part with absorber and bottom part with fuelled follower, the shift of maximum can be explained by the position of different parts of control rod inside the reactor core (see Figure 4b). In configuration when both CRs are partially withdrawn (R610, C481) in the bottom of the reactor core are only fuel follower parts of the CRs, which leads to more fissions in the bottom of the reactor core and consequently the maximum of the axial profile shifts to the lower axial position. We can also observe that when R CR is completely inserted and C CR is completely withdrawn (R896, C200) the maximum of the axial profile is approximately in the middle of the active fuel part, which is at -324 mm. From Figure 4b can be seen that in this configuration (R896, C200)) R CR has only absorber part and C CR has only fuel part inside the active fuel height. This configuration gives more homogeneous reactor core and therefore the maximum of the axial profile is approximately in the middle of the active fuel height.

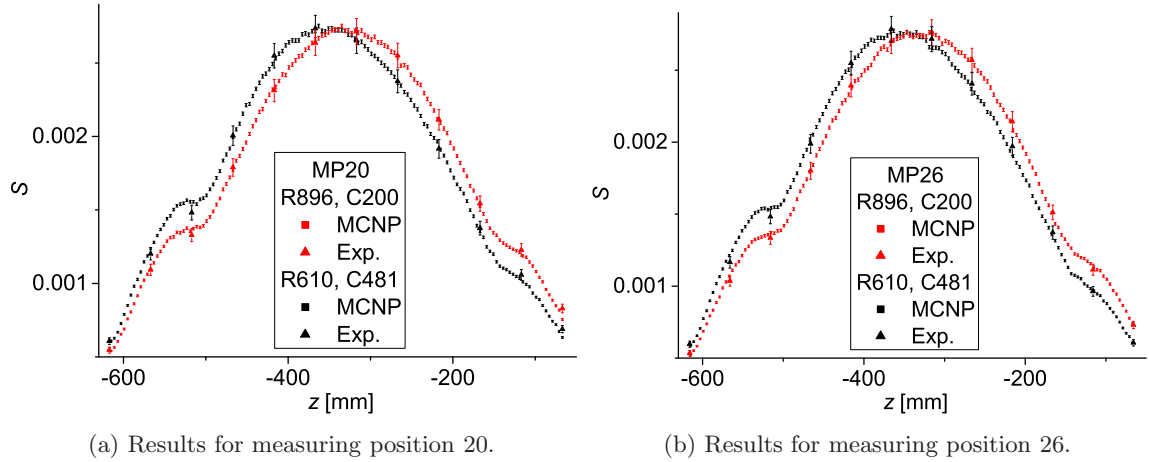


Figure 5: Comparison of fission rate axial profiles for MCNP calculations (squares) and experiment (triangles) at two different CR positions, red color represents R CR at position 896 and black color R CR position at 610. All distributions are normalized to the surface area below the graph. Error bars represent  $1\sigma$  statistical and measurement uncertainty.

It can also be deduced that the height of the neutron flux local maxima changes, however their axial position remains unchanged (approximately at -125 mm and -525 mm), this is supported by the fact that local maxima are a consequence of the upper and lower graphite inserts inside the fuel rod, which act as neutron reflector. The height of the individual local maximum can also be influenced by CR position. For the CR configurations when both CRs are only partially withdrawn (R610, C481) in Figures 4b, 5 and 6, as already explained the reactor core is more homogeneous and therefore both local maxima are approximately the same size. While for the CR configuration with completely inserted R CR (R896, C200) the local maximum in the lower part of the reactor core is relatively higher, because there is the fuel part of the CRs and local maximum on the higher axial position is relatively lower, due to the absorber part of the CRs.



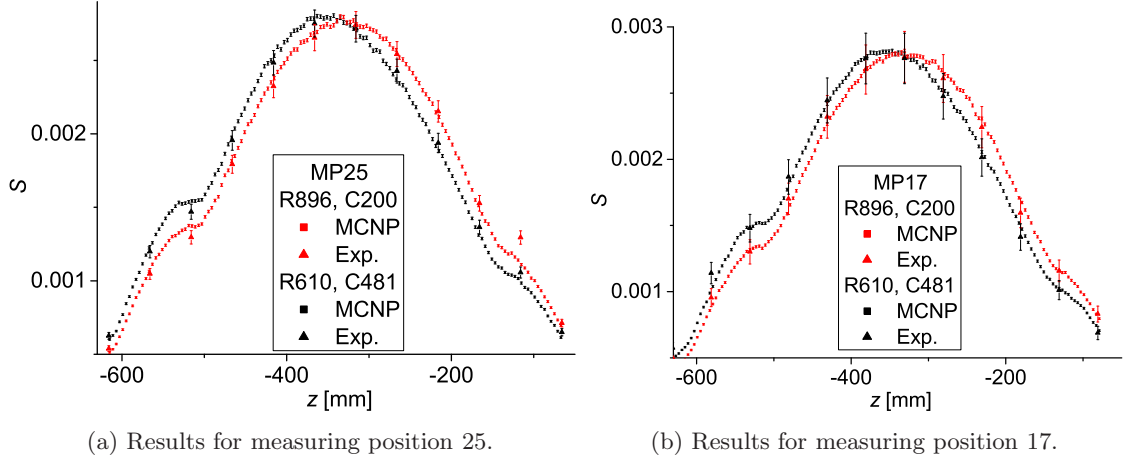


Figure 6: Comparison of fission rate axial profiles for MCNP calculations (squares) and experiment (triangles) at two different CR positions, red color represents R CR at position 896 and black color R CR position at 610. All distributions are normalized to the surface area below the graph. Error bars represent  $1\sigma$  statistical and measurement uncertainties.

For better visualization of deviations between calculations and experiment the  $\chi^2$  value and  $C/E-1$  was calculated for each axial profile and are reported for all measurements in Appendix A.1.

### 3.1.2. Control rod movement

When multiple detectors ( $n$ ) are placed inside the reactor core, their average signal can be calculated taking into account the correction factor due to the control rod movement. The value of the correction factor depends on the CR configuration and the detector position inside the reactor core. In the optimal detector position the correction factor would be similar to 1, in such location the CR movement has minimal effect on the detector signal.

Comparison of measurements with calculations was possible at any measuring axial position ( $z_i$ ) for different R CR positions ( $m$ ). Measured detector response ( $N(z_i, n, m)$ ) was further corrected with the response of a reference ex-core detector ( $f(m)$ ), which is a compensated ionisation chamber inside the linear channel with signal linearly proportional to the thermal neutron flux. Its response for individual CR configuration ( $m$ ) was evaluated by MCNP calculations. In the end measurements were normalized to the average over different CR positions as (Kaiba et al., 2015):

$$P(z_i, n, m) = \frac{N_i(n, m)}{N_{0,i}(n)}, \quad N_i(n, m) = N(z_i, n, m)f(m), \quad N_{0,i}(n) = \frac{\sum_m^M N_i(n, m)}{M}, \quad (3)$$

where  $M$  represents total number of different R CR positions and  $P(z_i, n, m)$  is the measurement normalized to the average over different R CR positions.

The MCNP calculations ( $N^c(z_i, n, m)$ ) were normalized according to Eq. (1). Due to the constant reactor power and relative comparison of results only normalization to the calculated  $k_{eff}(m)$  value for individual CR configuration ( $m$ ) (Žerovnik et al., 2014b) and to the average value over different CR configurations ( $N_{0,i}^c(n)$ ) was applied as:

$$P^c(z_i, n, m) = \frac{N_i^c(n, m)}{N_{0,i}^c(n)}, \quad N_i^c(n, m) = \frac{N^c(z_i, n, m)}{k_{eff}(m)}, \quad N_{0,i}^c(n) = \frac{\sum_m^M N_i^c(n, m)}{M}, \quad (4)$$

where  $n$  stands for individual detector,  $M$  represents total number of different CR configurations and  $P^c(z_i, n, m)$  is calculation normalized to the average over different CR configurations.

The comparisons of MCNP calculations with measurements in MP20 and MP25 are presented in Figure 7 and the comparisons of MP26 and MP17 in Figure 8 at the detector axial positions -215 mm, -315 mm and -415 mm relative to the upper part of the upper grid above the active fuel part of the reactor core. The Figures 7 and 8 represent the dependence of the correction factor on the detector axial position as a function of different R CR positions.

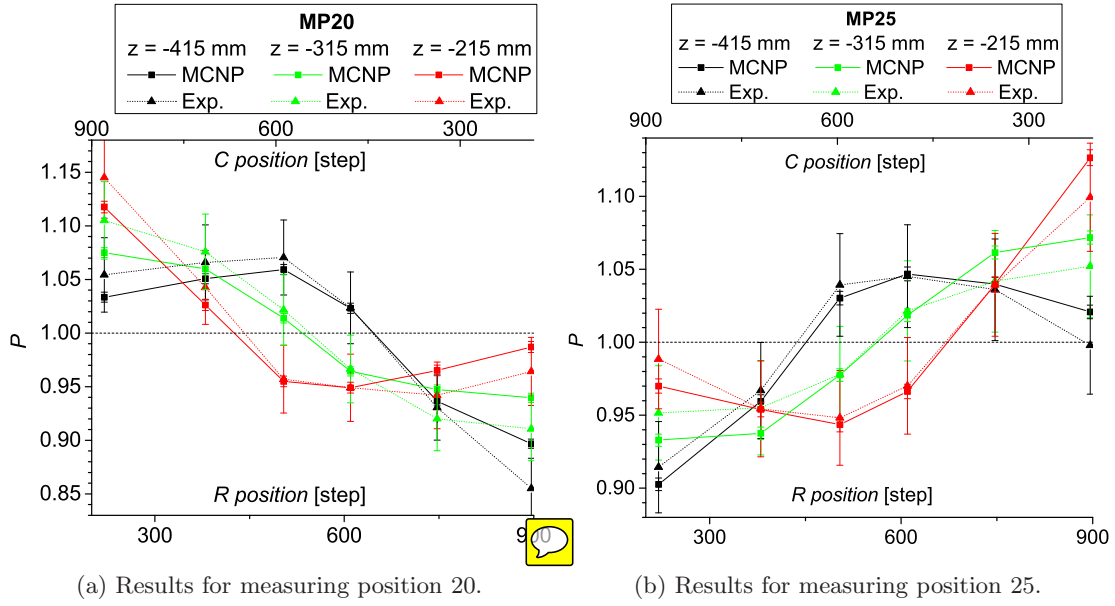


Figure 7: Comparison of MCNP calculations (squares) and experiment (triangles) as a function of R control rod position. Connecting line (full for MCNP and dotted for measurements) serves as an eye-guide only.

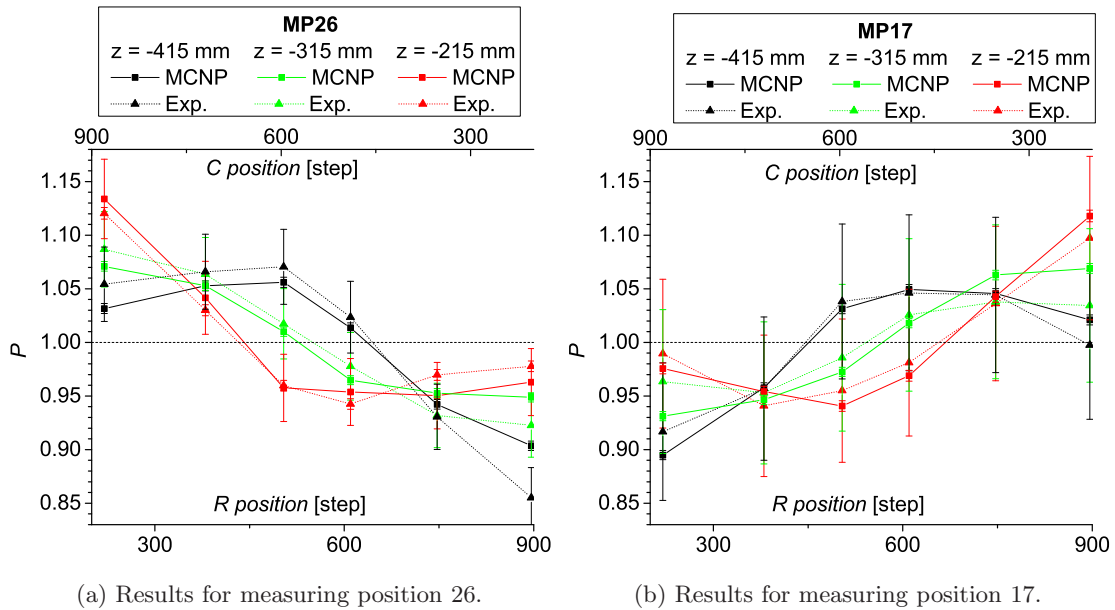


Figure 8: Comparison of MCNP calculations (squares) and experiment (triangles) as a function of R control rod position. Connecting line (full for MCNP and dotted for measurements) serves as an eye-guide only.

The agreement between the measurements and the MCNP calculations is relatively good, with deviations within the uncertainties. The agreement is better when R CR is in partially withdrawn/inserted position, where the normalized measured or calculated value is closer to 1. The calculations deviate more from the measurements at the R CR position closely to the fully withdrawn (step 181) or fully inserted (step 900). Measurements confirm assumption that for positions of CRs closer to the fully withdrawn/inserted position the above mentioned correction factor should be used. We can also observe that the detector signal in axial position close to the middle of the active fuel

height (green color) deviates the least between different CR configurations.

In Figure 9 the comparison between MP25 and MP26 and between MP20 and MP17 is shown. The difference between those measuring positions is due to their different positions inside the reactor core and therefore represents the effect of radial detector position on the correction factor. MP25 and MP17 are near the C CR, while MP26 and MP20 are closer to the R CR. Configuration with R CR fully inserted and consequently C CR fully withdrawn leads to the decrease in the relative detector response in MP26/MP20 and increase in MP25/MP17. We can also observe that the detector response in both MPs have the same value when both control rods (R and C) are in approximately the same position around step 540.

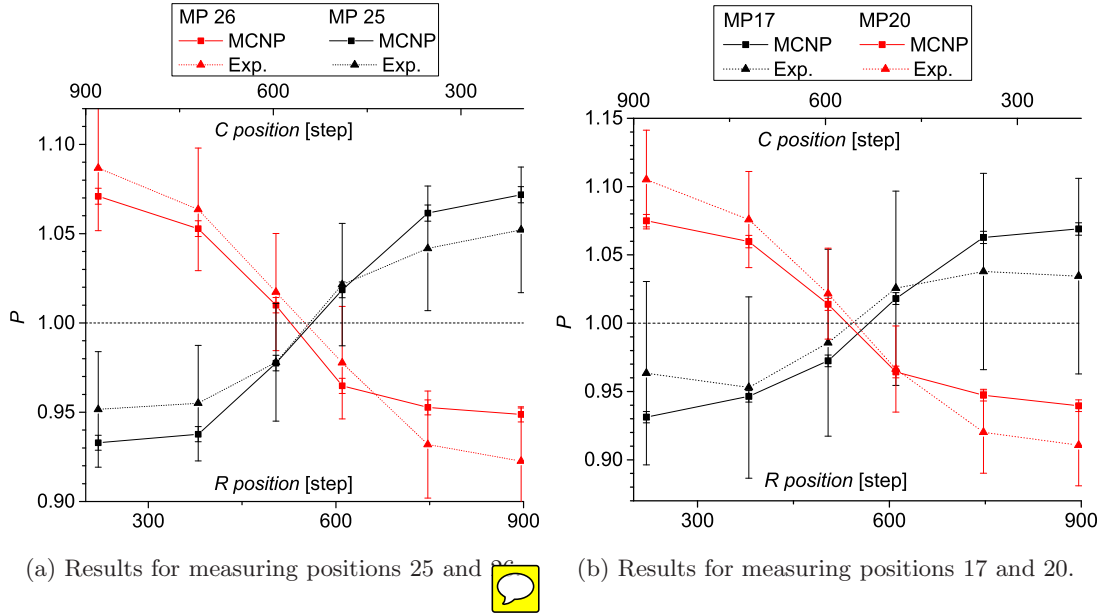


Figure 9: Comparison of MCNP calculations (squares) and experiment (triangles) as a function of R control rod position at fixed axial position -315 mm. Connecting line (full for MCNP calculations and dotted for measurements) serves as an eye guide only.

### 3.2. Second experimental set

Contrary to the first set of experiments, in the second set only two FCs were moving axially through the reactor core and the third FC was at a fixed axial position. FCs were positioned as shown in Figure 3b. Therefore the third FC in MP22 can be used as a reference detector for the second experimental set. Experimental and calculational CR positions are reported in Table 2.

#### 3.2.1. Axial shift

In first step axial profiles measured with two moving counters were normalized in the same way as it was performed for the first experimental set (see Section 3.1.1), without normalization to the reference counter. Scoping axial profiles in second set of experiments are represented in Figure 10. A constant axial shift between measured and calculated detector response can be observed. Due to lack of the measurement hole inside the bottom grid at MP5 and MP8 it was not possible to fix the guide tube at the bottom grid, inducing the uncertainty in the guide tube position and consequently the uncertainty in the FC position. Furthermore, it is also possible that aluminium guide tube bends at the lower reactor grid. The axial shift appears to be different between MP5 and MP8, but is approximately the same among different CR configurations. The evaluation of axial shift value was performed taking into account only measurements in axial positions inside the active fuel part, before local maximum due to the graphite plugs appears. Evaluation was performed using linear interpolation between calculations, which is justified due to a large number of calculation points. Measurements were manually shifted in steps of 1 mm and for each shift  $\chi^2$  value (see Appendix A) was calculated. The value of optimal axial shift was determined by finding minimum of calculated  $\chi^2$  values and was

averaged over different CR configurations. The individual axial shift was calculated for MP5 (-16 mm) and MP8 (-26 mm) and was applied in further evaluation.

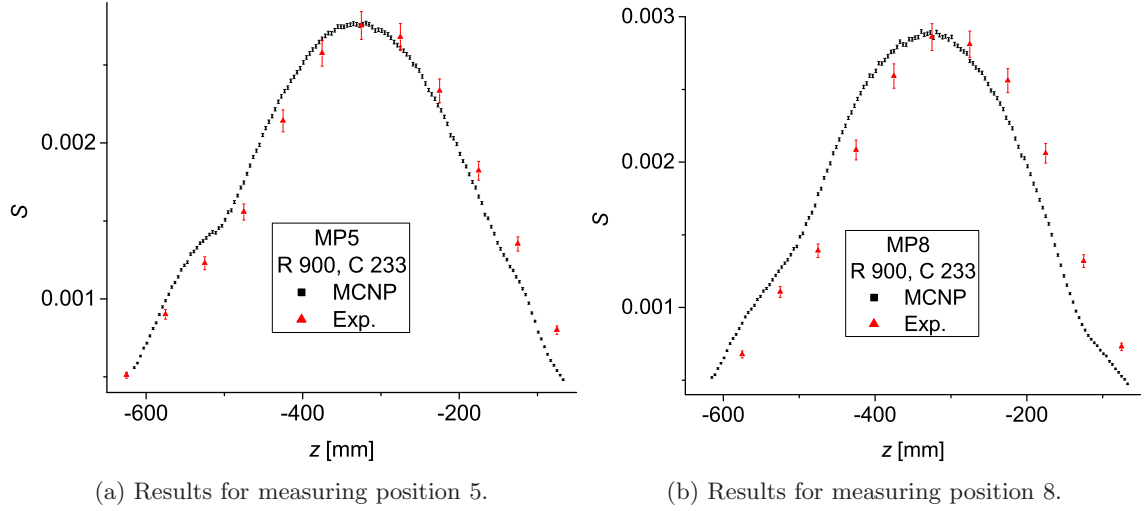


Figure 10: Comparison of fission rate axial profiles from MCNP calculations (dots) and experiment (triangles) at R CR position 900. All distributions are normalized to the surface area below the graph.

### 3.2.2. Normalization to the reference counter

Measurements in MP5 and MP8 were normalized to the response of the third FC positioned in MP22. For comparison of calculations the response of the reference counter was calculated in axial position approximately in the middle of the active fuel height. Because signals from different FCs are compared, also factor ( $K$ ) due to different FCs characteristics (e.g. mass of fissile deposit) should be taken into account. The value of this factor can be determined using measured ( $E$ ) and calculated ( $C$ ) values from first experimental set (see Section 3.1), where good agreement between measurements and calculations was already confirmed. For determination of normalization factor only measurements performed inside the active fuel height were taken (before local maximum in axial profile appears, where deviations between measurements and calculations are greater). If absolute comparison of measurements with calculations would be performed for the first experimental set, measurements should be multiplied with the normalization factor, which depends on calculation and FCs characteristics and therefore would not be the same if different FCs are in the same MP. Due to the good description of the experiment and the MCNP model, it is assumed that for the same FC this factor should be equal regardless to the CR configuration or detector MP. The normalization factor is equal to:

$$K_{j,m,z_i} = \frac{E_{j,m,z_i}}{C_{j,m,z_i}}, \quad (5)$$


where indices  $j$  and  $m$  represent individual FC and different CR configurations respectively and  $z_i$  represents  $i^{th}$  axial position. To enable comparison of calculations with measurements at exact measurement position, the linear interpolation between calculation points was used. For determination of one normalization factor for each FC, the average factor over all measured axial positions and CRs configurations was determined, taking into account  $k_{eff}$  value and ex-core detector response ( $f$ ) for individual calculation (Žerovnik et al., 2014b) (see Section 3.1.2).

$$K_j = \frac{1}{MU} \sum_m \sum_i K_{j,m,z_i} k_{eff,m} f(m), \quad (6)$$

where  $U$  and  $M$  represent the total number of measured axial positions and CRs configurations respectively. The normalization factor for each FC was calculated from experimental and calculation

values from first experimental set. The normalization value only depends on FC characteristics, therefore it can be used to normalize second experimental set to the reference counter. Normalized value of  $j^{\text{th}}$  counter (counter in MP5 or MP8)  $R_{j,m}$  at  $m^{\text{th}}$  CR configuration:

$$R_{j,m} = \frac{E_{j,m} K_3}{E_{3,m} K_j}, \quad (7)$$

where  $K_3$  and  $E_{3,m}$  represent the normalization factor and measurement for the third (reference) counter in MP22. Due to the comparison of experiments and calculation of both FCs at the same CRs configuration the  $k_{eff}$  and ex-core detector response for individual CR configuration average 

### 3.2.3. Axial profiles

Axial profiles in both MPs were obtained by taking into account both above mentioned corrections and can be seen in Figure 11.

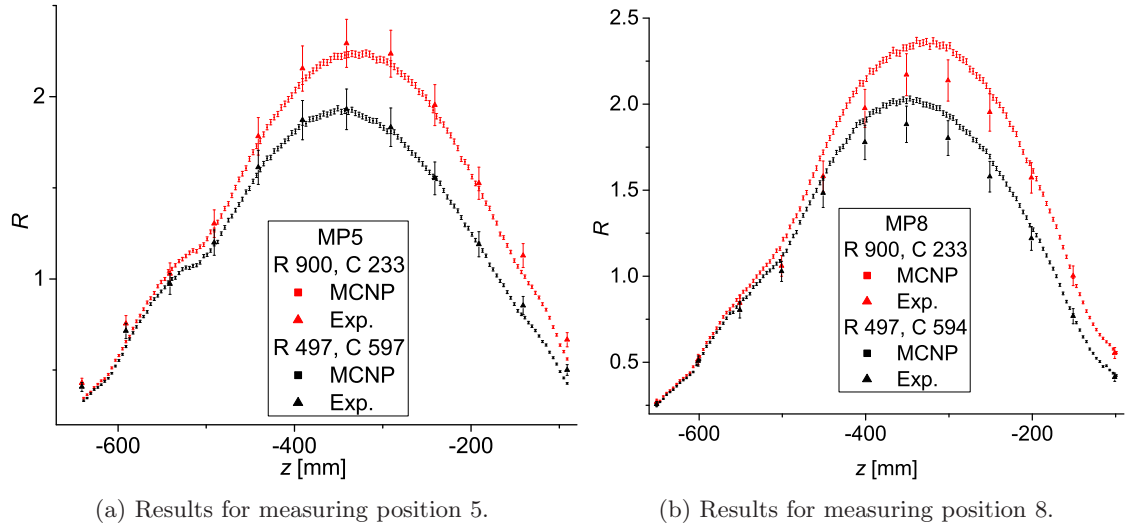


Figure 11: Fission rate axial profiles at R CR in position 900 (red) and in position 497 (black). Measurements are represented as triangles, while calculations are represented as squares. Error bars represent  $1\sigma$  statistical and measurement uncertainties.

The maximum in axial profile shifts similarly as observed for the first set of experiments. A similar effect on neutron flux local maxima as already explained above can also be confirmed here, but with lower effect. It can be seen that the top local maximum in axial profile is much smaller compared to the first experimental set. This is due to the different position of the detector inside the reactor core. MP5 and MP8 are very close to other two CRs (see Figure 3), which were fully withdrawn during whole experiment. When CR is completely withdrawn the upper part of the CR, which contains strong neutron absorber begins approximately at -250 mm (see Figure 4). Therefore the effect of graphite plugs inside the fuel pins is dominated by the effect of neutron absorption inside the CR absorber, which results in lowering the top local maximum in axial profile. The absorber part of CR does not effect the lower local maximum, which is still visible within the axial profile. Another thing we can observe is different maximum heights over different CR configurations. MP5 and MP8 lie symmetrically between R and C CRs and therefore their movement should have minimum effect on the detector signal in those MPs. The change in value of axial maximum is due to the normalization to the reference counter in MP22, which lies close to the R CR (see Figure 3b). When R CR is completely inserted (red color) the detector signal in MP22 is lower and therefore normalized value of other two detectors is bigger and decreases with withdrawal of R CR. This effect can not be seen in first experimental set due to the normalization to the integral below the graph.

Even though corrections to the measured signal were made, the deviation between measurements and calculations in MP8 are not within the uncertainties. However, the agreement is better in MP5

(within the active fuel part) with deviations within the uncertainties. More axial profiles are presented in Appendix A.2, where calculated  $\chi^2$  and  $C/E - 1$  values are reported. It should be noted that the agreement seems to be worse due to more challenging type of normalization and does not imply that the MCNP model of the reactor is deficient. If normalization is similar to the first experimental set (normalization to the integral and without normalization to the reference counter) the agreement would be comparable to the first experimental set. It can be concluded that when choosing appropriate reference position a great care must be put into correct normalization and evaluation of the detector signal.

### 3.2.4. Control rod movement

The effect of CR movement on the detector signal in positions MP5 and MP8 was analysed for two different types of normalization. For the first type of normalization the normalization to the reference counter was not performed and for the second type of normalization it was.

**3.2.4.1. First type of normalization.** This normalization is the same as for the first experimental set, without normalization to the reference counter and is represented as Figure 12. In this type of normalization pure impact of CR movement on the detector signal in MP5 and MP8 can be observed. We can see that the deviations are smaller compared to the MPs in first experimental set and correction factor is similar to 1.0, which means that CR movement has minimal effect on detector signal. Deviation between measurements and calculations are in general within the uncertainties.

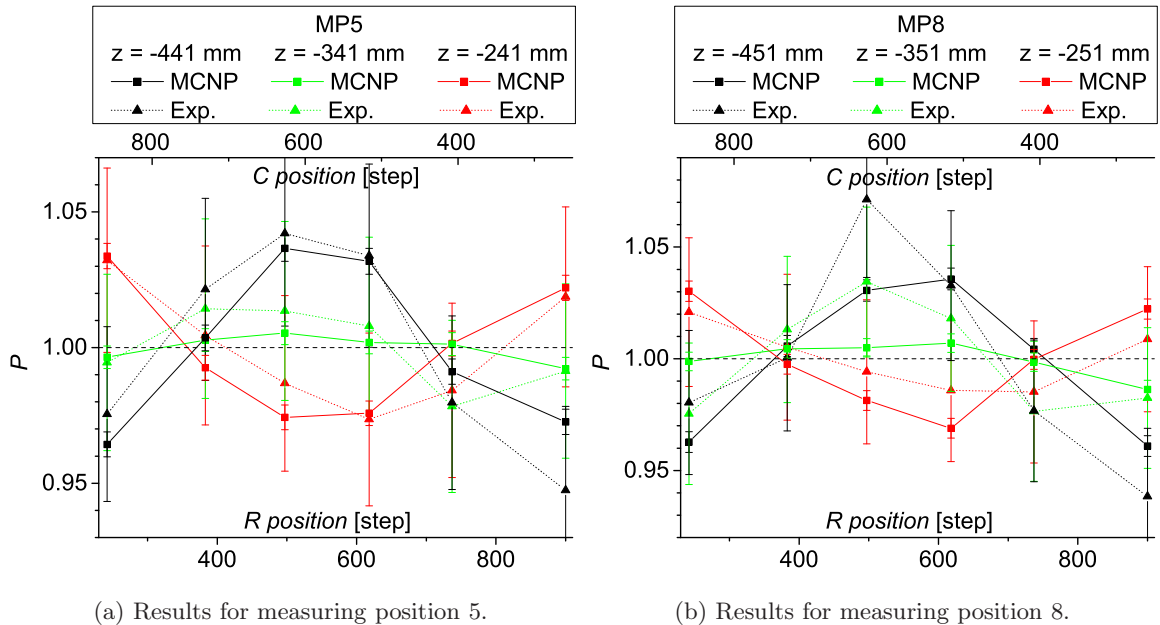


Figure 12: Comparison of MCNP calculations (squares) and experiment (triangles) as a function of R control rod position. Connecting line (full for MCNP and dotted for measurements) serves as an eye-guide only.

**3.2.4.2. Second type of normalization.** This normalization is taking into account the reference counter and is represented in Figure 13. The calculation procedure is the same as described in Eq. (3), except that this time  $N$  represents normalized calculated or measured value ( $R$ , see Eq. (7)) to the reference counter. We can observe that deviations between different CR configurations are bigger compared to first type of normalization, this is due to the response of the reference detector in MP22, which is close to the R CR. In this case the correction factor due to the CR movement should be taken into account. It can be concluded that reference detector position was not optimal for normalization.

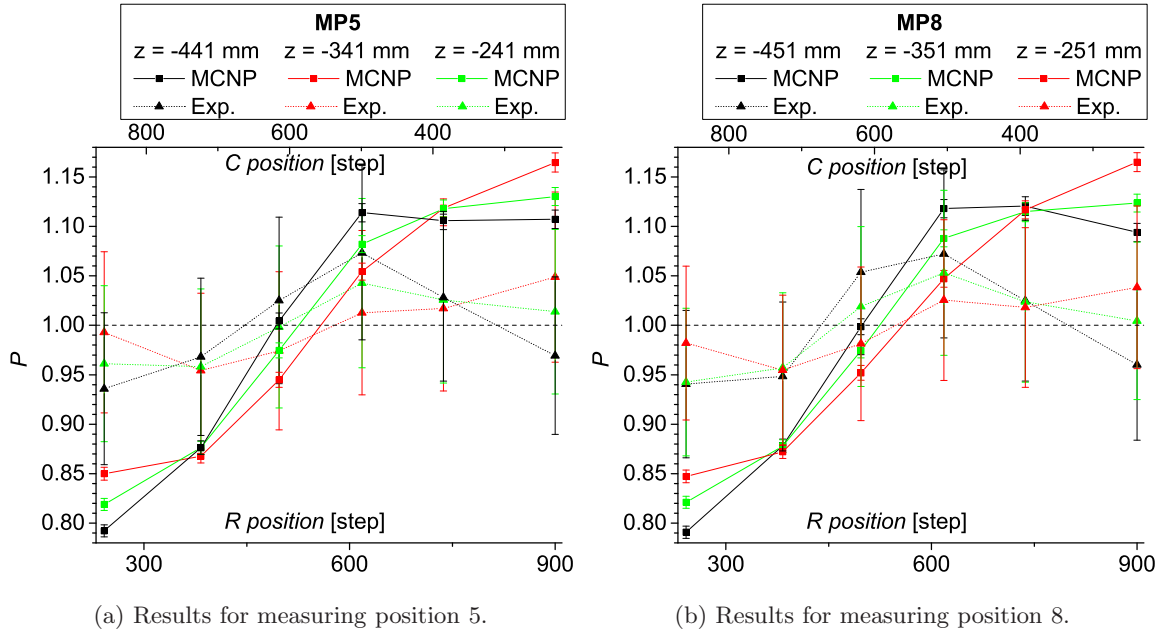



Figure 13: Comparison of MCNP calculations (squares) and experiment (triangles) as a function of R control rod position. Connecting line (full for MCNP and dotted for measurements) serves as an eye-guide only.

#### 4. Core mapping

Following the successful validation of the computational model for fission rate profiles, the model has been used for tallying the fission rate and neutron flux throughout the entire reactor core. Consequently, a wide variety of 2D flux and fission rate maps was formed. In Figures 14 and 17 the changes in fission rate and neutron flux in the  $xy$  plane approximately at the center of the active fuel height are represented. A similar 2D map can also be presented at different axial positions or at different  $(xz, yz)$  planes.

##### 4.1. Fission rate profile

Calculated fission rates were normalized using Eq. (1) for a 100 W reactor power to obtain absolute values. Normalized results are presented in Figure 14. The fission rate is roughly proportional to the thermal neutron flux and is the highest in the moderator between the fuel elements. The fission rate significantly decreases within the CR active volume. Due to the geometrical symmetry of the core (except the outer, F ring), the distribution is symmetrical regarding to the R axis.  CR swap.

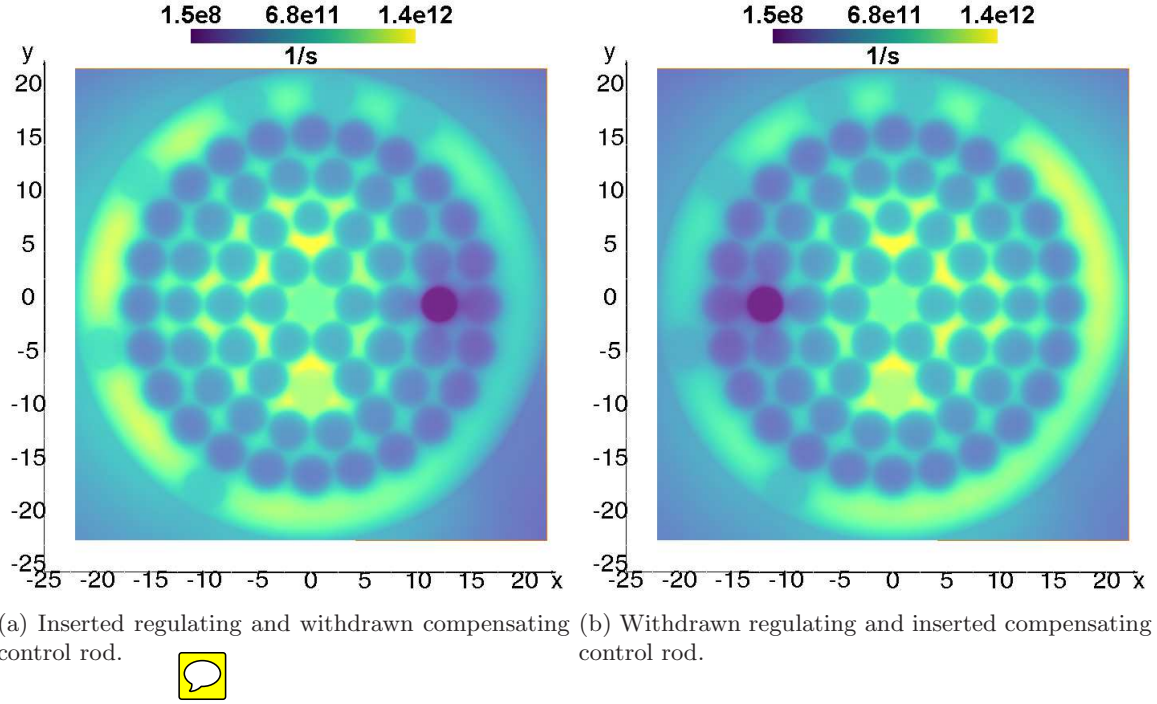


Figure 14: Fission rate profiles through the reactor core at the  $xy$  plane approximately at the center of the active fuel height. The fission rate values are represented with colors, ranging from high values represented in yellow (light) to low values represented in purple (dark).

#### 4.1.1. $\chi^2$ profile for fission rate

For evaluation of optimal detector response the  $\chi^2$  with respect to different CR positions as a function of detector position has been calculated throughout the entire reactor core, using the expression:

$$\chi^2(x_i, y_j, z_k) = \sum_m \left( \frac{N_{0,i,j,k} - N(x_i, y_j, z_k, m)}{\sigma_m} \right)^2, \quad (8)$$

where the sum is performed over different CR configurations. The symbol  $N$  is now a function of 3 spatial coordinates and therefore  $N(x_i, y_j, z_k, m)$  represents calculated  $^{235}\text{U}$  fission rates in fixed position inside the reactor core at  $m^{\text{th}}$  CR configuration and  $\sigma_m$  represents statistical uncertainty of the individual  $N(x_i, y_j, z_k, m)$ .  $N_{0,i,j,k}$  stands for average value of the calculated  $^{235}\text{U}$  fission rates at fixed position and over the different CR positions.

The  $\chi^2$  represents the deviations from the average value in desired detector position  $(x_i, y_j, z_k)$  the deviations from the average detector signal due to CR movement should be minimal and therefore the calculated  $\chi^2(x_i, y_j, z_k)$  should be minimized.

For evaluation of  $\chi^2$  for fission rate the  $N$  represents the fission rate values. The results of the  $\chi^2$  profile in  $xy$  plane, approximately in the middle of the active fuel height are represented in Figure 15. In Figure 15a the color-scale represents the total range of  $\chi^2$  values. Because we are searching for optimal detector position and therefore for minimal  $\chi^2$  the color-map range in Figure 15b was adjusted to represent lower values of  $\chi^2$ . From the Figure 15a we can observe that the largest deviations are around the CRs and other positions inside the reactor core have much lower deviation. When we lower the upper limit of color-map for about  $10\times$  we can observe that the smaller deviations appear further away from the CRs around the middle of the reactor core. For better visualization of lower values of  $\chi^2$ , the original color-map range was shrunk for  $500\times$ . In Figure 16 all 3 plane views are represented approximately in the middle of the reactor core. We can observe that the most appropriate detector position lies approximately in the middle of the active fuel height and on the central core symmetrical.



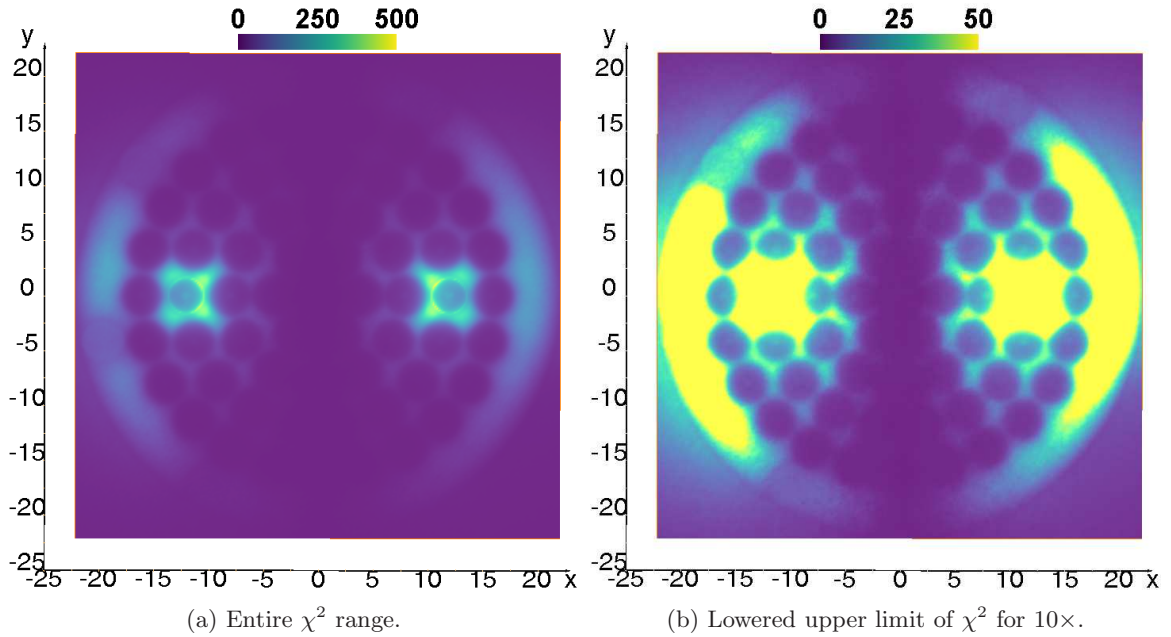


Figure 15:  $\chi^2$  profile of fission rate is represented at different ranges.

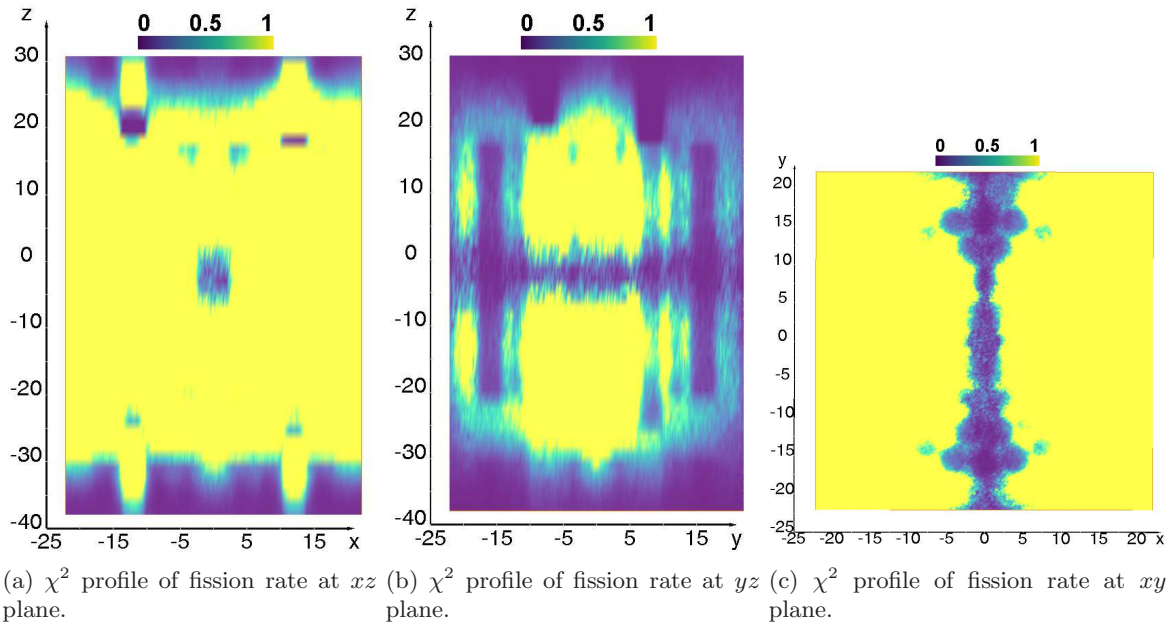
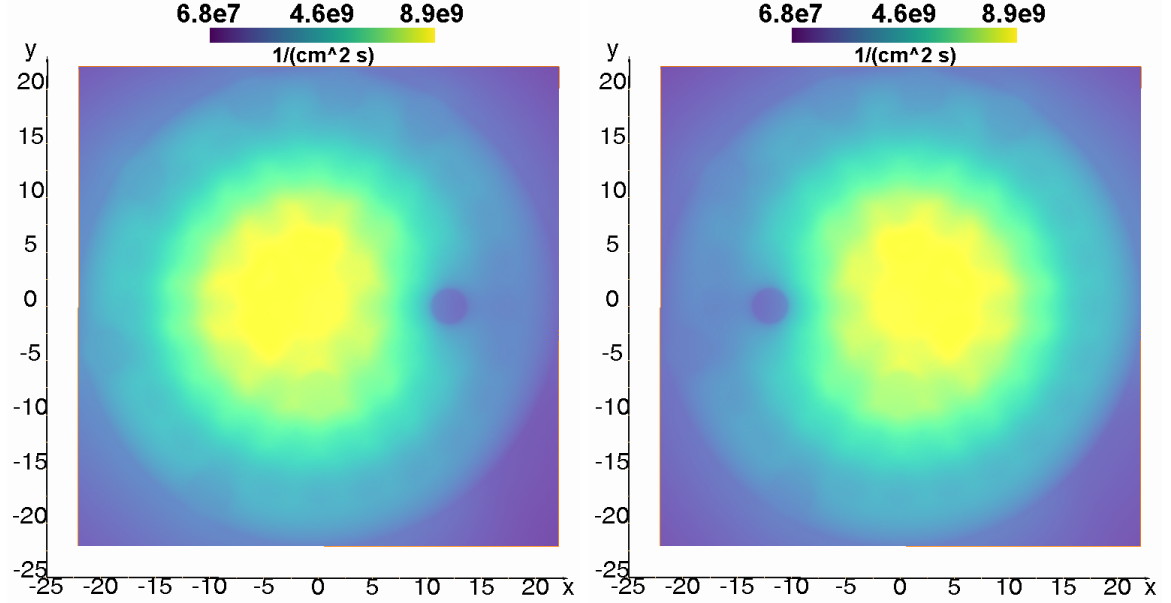


Figure 16: All planes are represented approximately in the middle of the reactor core. Values of  $\chi^2$  are represented in colors ranging from low values in purple (dark) to high values in yellow (light).

#### 4.2. Neutron flux profile

Results for neutron flux obtained with the MCNP were normalized also using Eq. (1) for a 100 W reactor power to obtain absolute values. Complementary to the fission rate the energy integrated (total) neutron flux was also been tailed through the entire reactor core. Contrary to the fission rate, the variations in the total flux (Figure 17) between the fuel and moderator regions are much smaller, while the flux expectedly decreases towards the edge of the core. The same as the fission rate, also the

neutron flux significantly decreases within the CR active volume. Due to the geometrical symmetry of the core (except the outer, F ring), the distribution is symmetrical regarding to the R and C CR swap.



(a) Inserted regulating and withdrawn compensating control rod. (b) Withdrawn regulating and inserted compensating control rod.

Figure 17: Neutron flux profiles throughout the reactor core at the  $xy$  plane approximately at the center of the active fuel height. The left figure represents inserted and the right figure withdrawn R CR. The neutron flux values are represented with colors, ranging from high values represented in yellow (light) to low values in purple (dark).

#### 4.2.1. $\chi^2$ profile for neutron flux

For calculating the  $\chi^2$  profile for neutron flux through the entire reactor core the Eq. (8) was used, where on contrary to the fission rate the  $\phi(x_i, y_j, z_k, m)$  now represents the neutron flux value at fixed position at  $m^{\text{th}}$  CR configuration and  $N_{0,i,j,k}$  stands for the average value of neutron flux at fixed position over all CR configurations. The results are represented in Figures 18 and 19. In Figure 18 the  $xy$  plane of the reactor core, approximately in the middle of the active fuel height, is shown at different  $\chi^2$  color-map scales. In Figure 18b we can observe that the greatest deviations in the neutron flux are near the CRs and in further away from the CRs the  $\chi^2$  values seem at least an order of magnitude lower. In Figure 18b we can observe that the positions on the same distance from the CR have similar  $\chi^2$  value, which supports the assumption that optimal detector position should be further away from the CR movement.

For better understanding how the  $\chi^2$  profile of the neutron flux changes inside the reactor core the color-map scale was adjusted in a way to show lower values, where positioning neutron detector would be optimal. In Figure 19 all plane views are represented approximately in the middle of the reactor core with color-map upper limit lowered for  $\sim 1000\times$ .

Evaluating  $\chi^2$  profiles for both fission rate and total flux we can draw the same conclusion about the optimal detector position. From the Figures 16a and 19a we can evaluate that the optimal detector axial position is around the middle of the active fuel height. From Figures 16c and 19c can be concluded that positions lying on the vertical reactor core symmetrical have lowest  $\chi^2$  values and therefore are the most appropriate for positioning of in-core detector. Those positions are the most suitable due to their equal distance from R and C CRs, which leads to averaging of redistributions due to the movement of both CRs. From the Figure 16b and 19b the  $yz$  plane on the vertical reactor symmetrical can be observed. On the  $yz$  plane view the best detector positions are shown.

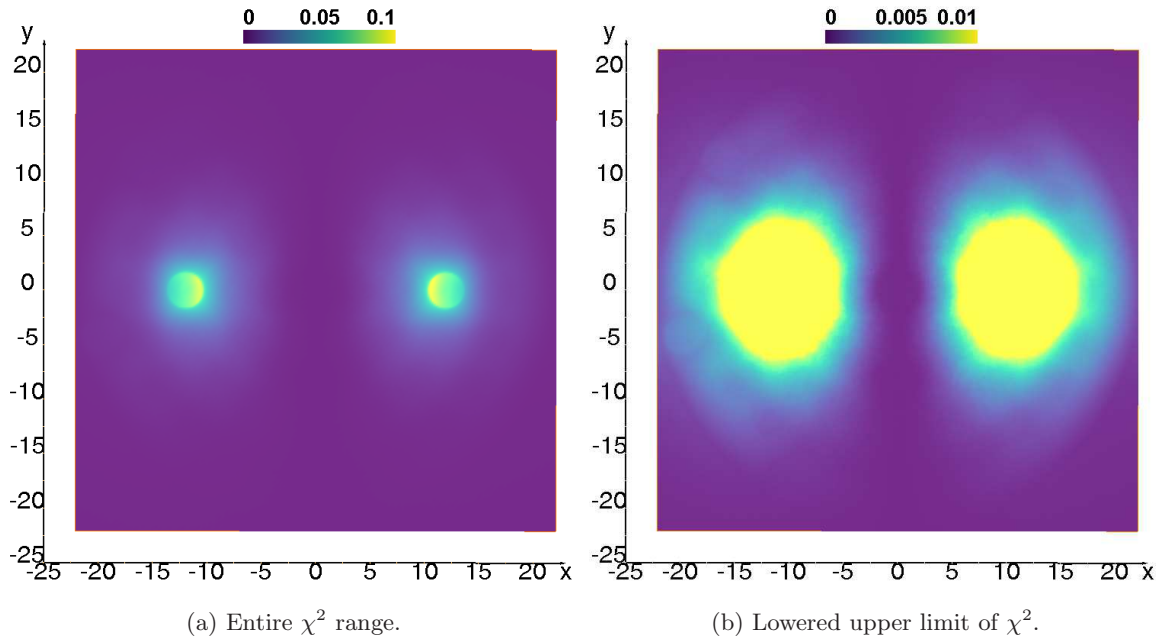


Figure 18:  $\chi^2$  profile of neutron flux is represented at different ranges. On left side the whole range of  $\chi^2$  is represented and on right figure the upper limit was lowered for better presentation of lower range values of  $\chi^2$ .

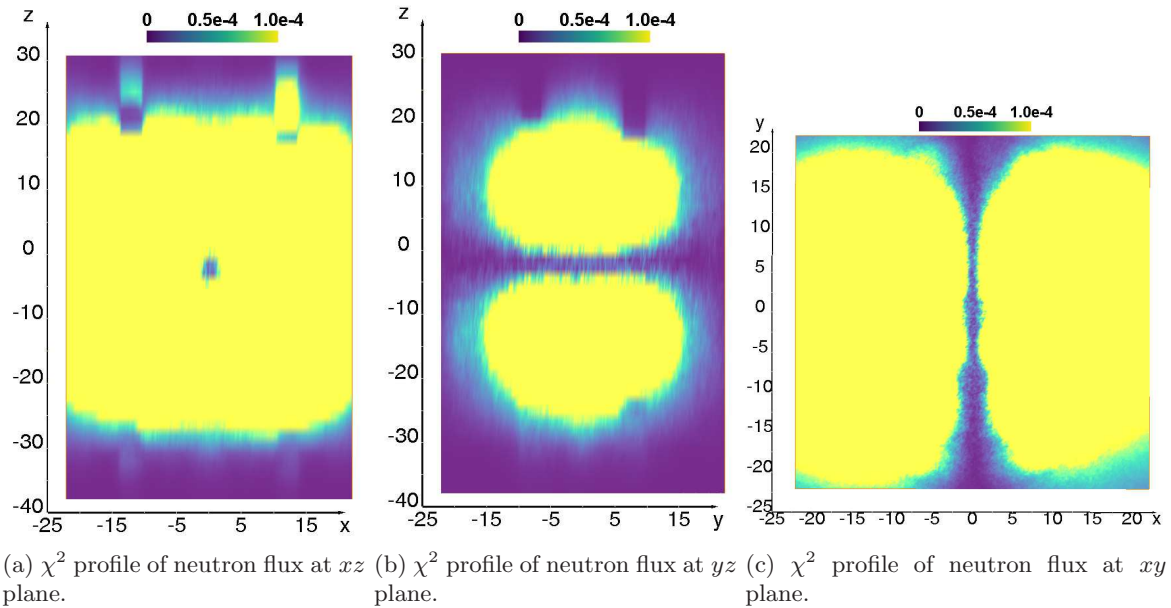



Figure 19: All planes are represented approximately in the middle of the reactor core. Values of  $\chi^2$  are represented in colors ranging from low values in purple (dark) to high values in yellow (light).

## 5. Conclusions

For improving the power monitoring system at the JSI TRIGA reactor the new system using multiple in-core FCs was proposed. Within the bilateral project between the JSI and CEA Cadarache many different measurements using multiple in-core FCs were performed and evaluated. In general

there is a good agreement between measurements and calculations, which additionally confirms the existing JSI TRIGA MCNP model. To average out the effects of neutron flux redistribution due to the control rod movement, the average detector signal can be calculated taking into account the correction factors. Even better possibility is to place the neutron detector in the position where effects of neutron flux redistribution are minimal. It was found out that the most appropriate measuring position for neutron detection would be on the vertical central line between the R and C CR approximately in the middle of the active fuel height. Among available MPs on the vertical central line, also experimental challenges must be taken into account. As represented in this paper, due to the unique configuration of MP5 and MP8, they are not the most suitable options. In future projects also other possible MPs and different types of fission chambers will be considered. 

## Acknowledgements

The research is funded by the bilateral project “Experimental verification of neutron flux form factors and Qualification of a new wide range multichannel neutron instrumentation” between the Ministry of education, science and sport of the Republic of Slovenia and Commissariat à l’énergie atomique et aux énergies alternatives (CEA) under contract number Q2-0012 1000-13-0106.

## References

- Aghara, S., Charlton, W., 2006. Characterization and quantification of an in-core neutron irradiation facility at a TRIGA II research reactor. *Nucl. Instr. Meth. B* 248, 181-190.
- Chadwick, M.B., et al., 2011. ENDF/B-VII.1 Nuclear Data for Science and Technology: Cross Sections, Covariances, Fission Product Yields and Decay Data. LA-UR 11-05121, Los Alamos National Laboratory, also: Nuclear Data Sheets, 112 Issue 12, pg. 2887-2996 (Dec 2011).
- Chiesa, D., et al., 2015. Measurement and simulation of the neutron flux distribution in the TRIGA Mark II reactor core. *Annals of Nuclear Energy*, 85, pg. 925-936 (Nov 2015). doi:10.1016/j.anucene.2015.07.011.
- Cindro, V., Kramberger, G., Lozano, M., Mandić, I., Mikuž, M., Pellegrini, G., Pulko, J., Ullan, M., Zavrtnik, M., 2009. Radiation damage in p-type silicon irradiated with neutrons and protons. *Nucl. Instr. Meth. A* 599 (1), 60-65.
- Geslot, B., Berhouet, F., Oriol, L., Breaud, S., Jammes, C., Filliatre, P., Villard, J.-F., 2009. Development and manufacturing of special fission chambers for in-core measurement requirements in nuclear reactor. In: *Proceedings of the International Conference Advancements in Nuclear Instrumentation Measurements Methods and their Applications (ANIMMA) 2009*, Marseille, France. IEEE Catalog Number: CFP0924I-CDR #111.
- Goorley, T., et al., 2012. Initial MCNP 6 Release Overview. LA-UR-11-07082, Los Alamos National Laboratory, also *Nuclear Technology*, 180, pp. 298-315 (Dec 2012).
- Huseynov, E., Garibov, A., Mehdiyeva, R., 2015. Effect of neutron flux, temperature and frequency on the permittivity of nanocrystalline silica. *Int. J. Mod. Phys. B* 28, 1450213 (2014) [14 pages] doi: <http://dx.doi.org/10.1142/S0217979214502130>
- Huseynov, E., Garibov, A., Mehdiyeva, R., 2015. Influence of neutron irradiation and temperature on the electric conductivity of SiO<sub>2</sub> nanoparticles. *Journal of Electrostatics*, 74 (2015), pp. 7378.
- Huseynov, E., Garibov, A., Mehdiyeva, R., 2015. TEM and SEM study of nano SiO<sub>2</sub> particles exposed to influence of neutron flux. *Journal of Materials Research and Technology*, 2015.
- ICSBEP, 2009. *International Handbook of Evaluated Critical Safety Benchmark Experiments*, Organization for Economic Cooperation and Development - Nuclear Energy Agency, NEA/NSC/DOC(95)03, Paris, published on DVD, ISBN 978-92-64-99054-8.

- Jeraj, R., Ravnik, M., 1999. TRIGA Mark II Reactor: U(20) – Zirconium Hydride Fuel Rods in Water with Graphite Reflector, IEU-COMP-THERM-003, International Handbook of Evaluated Critical Safety Benchmark Experiments, Organization for Economic Cooperation and Development – Nuclear Energy Agency, NEA/NSC/SOC(95)03, Paris, 1999.
- Jonah, S.A., Umar, I.M. , Oladipo, M.O.A., Balogun, G.I., Adeyemo, D.J., 2006. Standardization of NIRR-1 irradiation and counting facilities for instrumental neutron activation analysis. *Appl. Radiat. Isot.* 64, 818-822.
- Kaiba, T., et al., 2015. Validation of neutron flux redistribution factors in JSI TRIGA reactor due to control rod movements. *Appl. Radiat. Isot.*, 104 (2015), pp. 34-42. doi:10.1016/j.apradiso.2015.06.026.
- Kovačević, I., Pivac, B., Jačimović, R., Khan, M.K., Markevich, V.P., Peaker, A.R., 2010. Defects induced by irradiation with fast neutrons in n-type germanium. *Materials Science in Semiconductor Processing* 9, issues 4-5, 2006, pp. 606-612.
- Kramberger, G., Batič, M., Cindro, V., Mandić, I., Mikuž, M., Zavrtanik, M., 2007. Annealing studies of effective trapping times in silicon detectors. *Nucl. Instr. Meth. A* 571, 608-611.
- Kramberger, G., Cindro, V., Mandić, I., Mikuž, M., Milovanović, M., Zavrtanik, M., Žagar, K., 2010. Investigation of irradiated silicodetectors. *IEEE Trans. Nucl. Sci.* 57 (4), 2294-2302.
- Lin, X., Henkelmann, R., Türler, A., Gerstenberg, H., De Corte, F., 2006. Neutron flux parameters at irradiation positions in the new research reactor FRM-II. *Nucl. Instr. Meth. A* 564, 641-644.
- Meftah, B., Zidi, T., Bousbia-Salah, A., 2006. Neutron flux optimization in irradiation channels at NUR research reactor. *An. Nucl. Ene.* 33, 1164-1175.
- Merz, S., Djuricic, M., Villa, M., Böck, H., Steinhauser, G., 2011. Neutron flux measurements at the TRIGA reactor in Vienna for the prediction of the activation of the biological shield. *Appl. Radiat. Isot.*, article in press. doi: 10.1016/j.apradiso.2011.05.019.
- Radulović, V., Trkov, A., Jačimović, R., Jeraj, R., 2013. Measurement of the neutron activation constants  $Q_0$  and  $k_0$  for the  $^{27}\text{Al}(n,\gamma)^{28}\text{Al}$  reaction at the JSI TRIGA Mark II reactor. *J. Radioanal. Nucl. Chem.* 298, 1791-1800. doi: 10.1007/s10967-013-2596-6.
- Ravnik, M., Jeraj, R., 2003. Research reactor benchmarks. *Nucl. Sci. Eng.* 145, 145-152.
- Snoj, L., Ravnik, M., 2008. Power peakings in mixed TRIGA cores. *Nucl. Eng. Des.* 238 (9), 2473-2479.
- Snoj, L., Kavčič, A., Žerovnik, G., Ravnik, M., 2010. Calculation of Kinetic Parameters for Mixed TRIGA Cores with Monte Carlo. *An. Nucl. Ene.* 37 (2), 223-229. doi:10.1016/j.anucene.2009.10.020.
- Snoj, L., Kromar, M., Žerovnik, G., Ravnik, M., 2011. Advanced methods in teaching reactor physics. *Nucl. Eng. Des.* 241, 1008-1012.
- Snoj, L., Smodiš, B., 2011. 45 Years of TRIGA Mark II in Slovenia. In: *Proceedings of the International Conference Nuclear Energy for New Europe 2011*, Bovec, Slovenia, Paper no. 401.
- Snoj, L., Trkov, A., Jačimović, R., Rogan, P., Žerovnik, G., Ravnik, M., 2011. Analysis of neutron flux distribution for the validation of computational methods for the optimization of research reactor utilization. *Appl. Radiat. Isot.* 69, 136-141. doi: 10.1016/j.apradiso.2010.08.019.
- Stamatelatos, I.E., Varvayanni, M., Tzika, F., Ale, A.B.F., Catsaros, N., 2007. Monte Carlo simulation of the Greek Research Reactor neutron irradiation facilities. *Nucl. Instr. Meth. B* 263, 136-139.
- Štancar, Ž., Barbot, L., Domergue, C., Radulović, V., Trkov, A., Snoj, L., 2012. Evaluation of the Axial Absolute Power Profile Measurements at the JSI Triga Mark II Reactor. In: *Proceedings of the International Conference Nuclear Energy for New Europe 2012*, Ljubljana, Slovenia, Paper no. 1008.

- Štancar, Ž., Snoj, L., 2014. Thermal Power Calibration of the TRIGA Mark II reactor. In: Proceedings of the 23rd international conference Nuclear Energy for New Europe, Portorož, Slovenia, September, 2014.
- Štancar, Ž., Snoj, L., Barbot, L., Domergue, C., 2015. Evaluation of Fission Rate Profile Experimental Benchmark at the JSI TRIGA Mark II Reactor Using Monte Carlo Method. In: Proceedings of the Joint International Conference on mathematics and Computation (M&C), Supercomputing in Nuclear Applications (SNA) and the Monte Carlo (MC) Method, 19-23 April 2015, Tennessee, USA.
- Thévenin, M., Barbot, L., Corre, G., Woo, R., Destouches, C., Normand, S., 2014. Digital Real-Time Multiple Channel Multiple Mode Neutron Flux Estimation FPGA-based Device. In: Proceedings of the ISRD Conference, 18-23 May 2014, Aix en Provence, France.
- Trkov, A., Žerovnik, G., Snoj, L., Ravnik, M., 2009. On the self-shielding factors in neutron activation analysis. Nucl. Instr. Meth. A 610, 553-565. doi: 10.1016/j.nima.2009.08.079.
- Žerovnik, G., Snoj, L., Trkov, A., Barbot, L., Fourmentel, D., Villard, J.-F., 2014. Measurements of Thermal Power at the TRIGA Mark II Reactor in Ljubljana Using Multiple Detectors. IEEE Transactions on Nuclear Science 61, 2527-2531. doi: 10.1109/TNS.2014.2356014.
- Žerovnik, G., Podvratnik, M., Snoj, L., 2014. On normalization of fluxes and reaction rates in MCNP criticality calculations. An. Nucl. Ene. 63, 126-128. doi:10.1016/j.anucene.2013.07.045
- Žerovnik, G., Kaiba, T., Radulović, V., Jazbec, A., Rupnik, S., Barbot, L., Fourmentel, D., Snoj, L., 2015. Validation of the neutron and gamma fields in the JSI TRIGA reactor using in-core fission and ionization chambers. Appl. Radiat. Isot. 96, 27-35. doi:10.1016/j.apradiso.2014.10.026.

## Appendix A All fission rate axial profiles

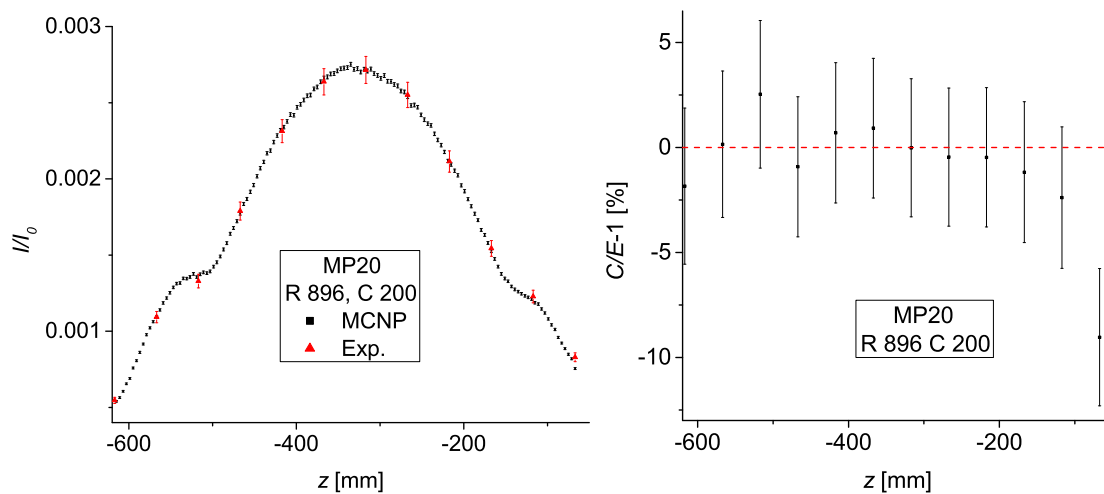
For evaluating the agreement between measurements and calculations the  $\chi^2$  value was calculated for individual experimental set and was normalized to number of measurements ( $U$ ). To enable a comparison at exact axial measuring positions, linear interpolation between adjacent calculation points was used. The use of linear interpolation is justified by a large number of calculation points. The agreement was therefore evaluated using following equation:

$$\frac{\chi^2}{U} = \frac{1}{U} \sum_i^U \left( \frac{E_i - C_i}{\sigma_i} \right)^2, \quad (9)$$

where  $E_i$  represent measured detector signal at axial position  $z_i$  and  $C_i$  represents calculated detector signal at the same axial position  $z_i$  using linear interpolation.  $\sigma_i$  stands for standard deviation for experiments. The agreement between measurements and calculations is considered to be good when  $\chi^2/U < 1$ . In captions of all axial profiles the corresponding  $\chi^2/U$  values are given (see Figures A.1-A.36). We can observe that in the first set the majority of calculations agree good with experiments, the only exceptions are 2 profiles measured in MP25 and the deviation is mainly due to the local maximum, which is consequence of the neutron reflector where calculations are not as accurate as in the active fuel part of the core. However in the second set, the agreement is not good in any CR configuration, due to different type of normalization.

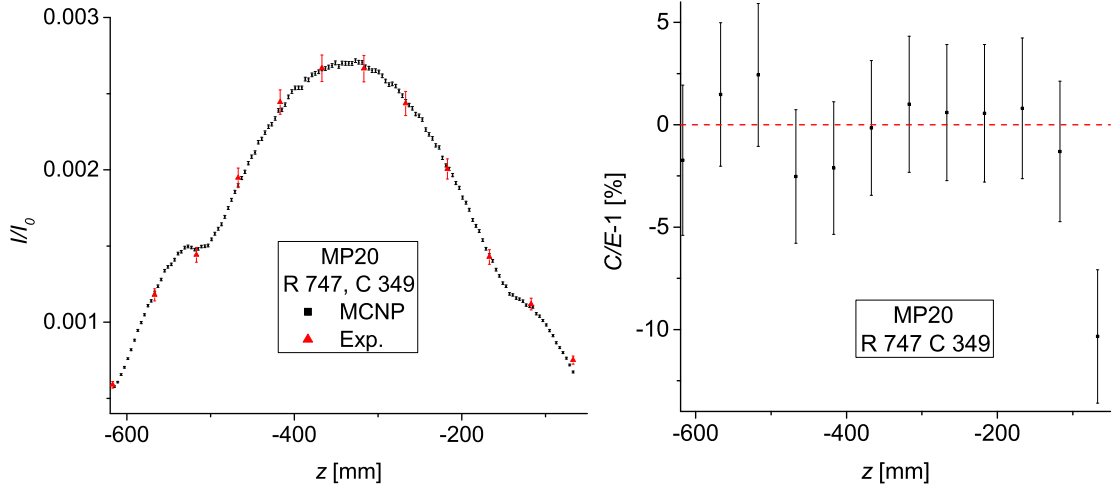
For better visualization of deviations between calculations and experiment also  $C/E - 1$  graphs are shown on right hand-side Figures A.1-A.36. The uncertainty was determined taking into account uncertainty in experiment and statistical uncertainty in MCNP calculation and also the normalization uncertainty in second experimental set.

### A.1 First set



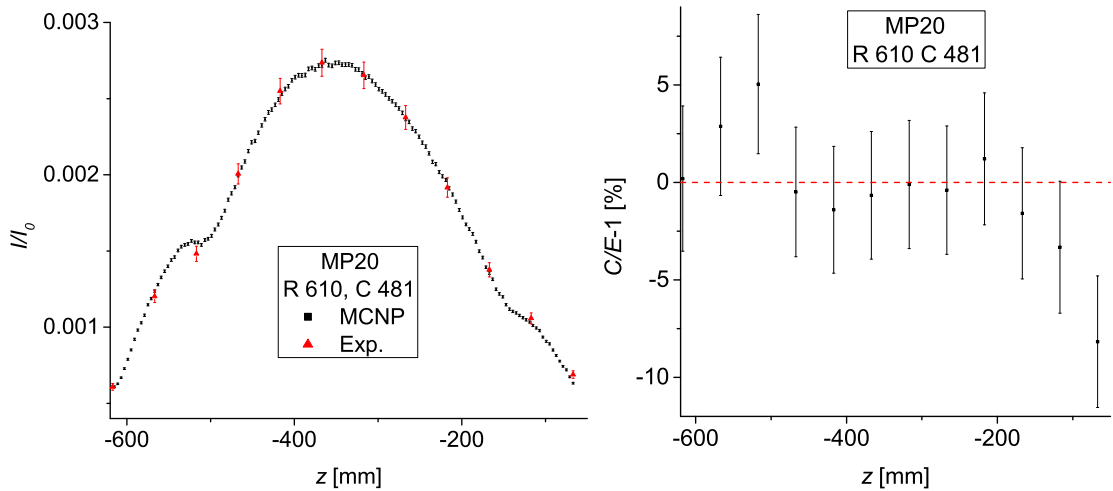
(a) Fission rate axial profile. Measurements are represented as triangles, while calculations are represented as squares. Error bars represent 1 $\sigma$  statistical and measurement uncertainties. (b) The deviation between experiment (E) and calculations (C). Error bars present uncertainty that was derived by taking into account 1 $\sigma$  statistical and measurement uncertainties.

Figure A.1: Measured and calculated fission rate in MP20 at R CR in position 896. The corresponding calculated  $\chi^2/U = 0.697$ .



(a) Fission rate axial profile. Measurements are represented as triangles, while calculations are represented as squares. Error bars represent  $1\sigma$  statistical and measurement uncertainties. (b) The deviation between experiment (E) and calculations (C). Error bars present uncertainty that was derived by taking into account  $1\sigma$  statistical and measurement uncertainties.

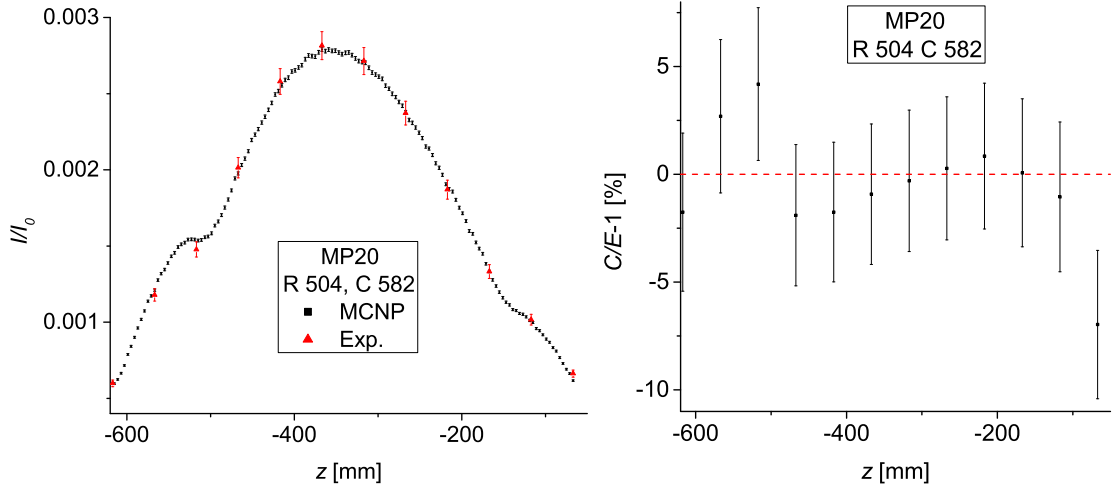
Figure A.2: Measured and calculated fission rate in MP20 at R CR in position 747. The corresponding calculated  $\chi^2/U = 0.908$ .



(a) Fission rate axial profile. Measurements are represented as triangles, while calculations are represented as squares. Error bars represent  $1\sigma$  statistical and measurement uncertainties. (b) The deviation between experiment (E) and calculations (C). Error bars present uncertainty that was derived by taking into account  $1\sigma$  statistical and measurement uncertainties.

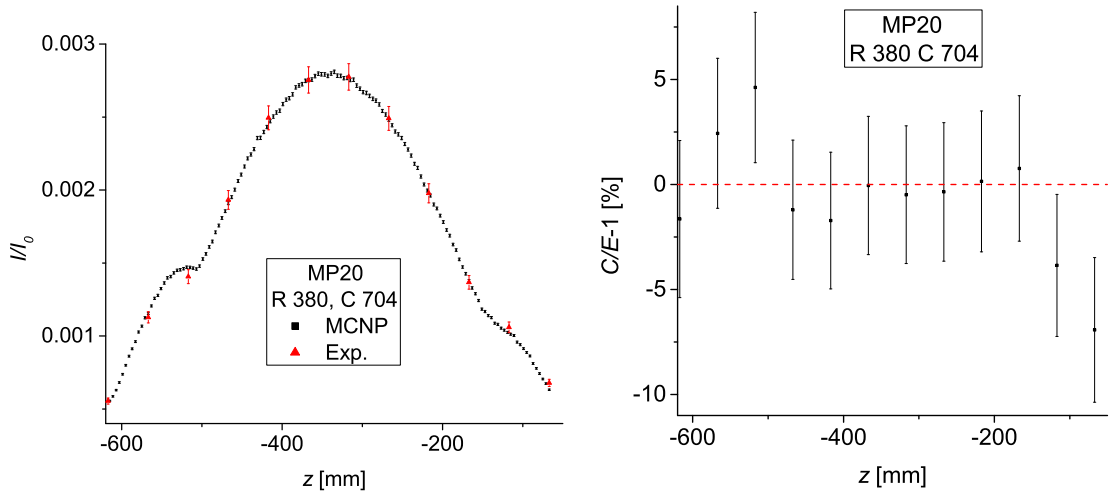
Figure A.3: Measured and calculated fission rate in MP20 at R CR in position 610. The corresponding calculated  $\chi^2/U = 0.817$ .





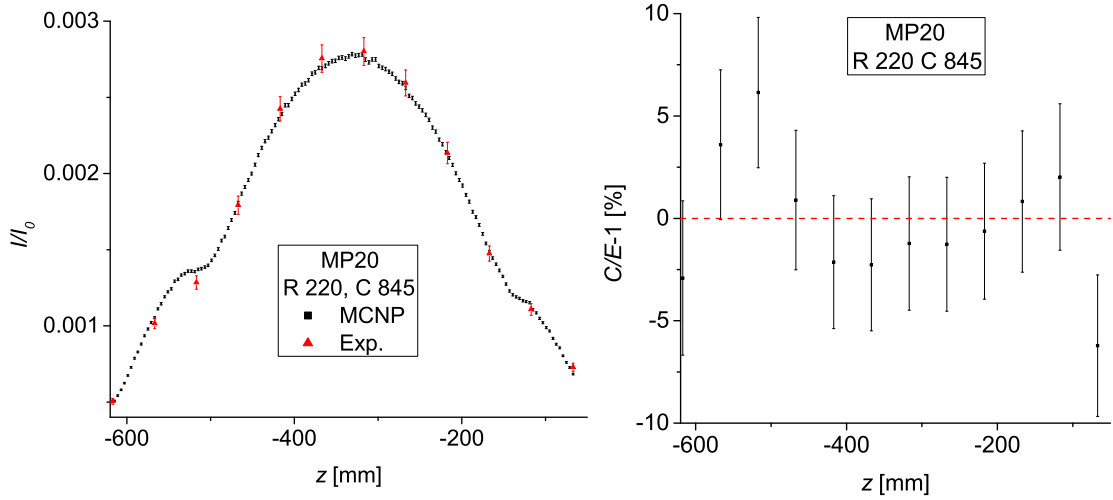
(a) Fission rate axial profile. Measurements are represented as triangles, while calculations are represented as dots. Error bars represent  $1\sigma$  statistical and measurement uncertainties. (b) The deviation between experiment (E) and calculations (C). Error bars present uncertainty that was derived by taking into account  $1\sigma$  statistical and measurement uncertainties.

Figure A.4: Measured and calculated fission rate in MP20 at R CR in position 504. The corresponding calculated  $\chi^2/U = 0.588$ .



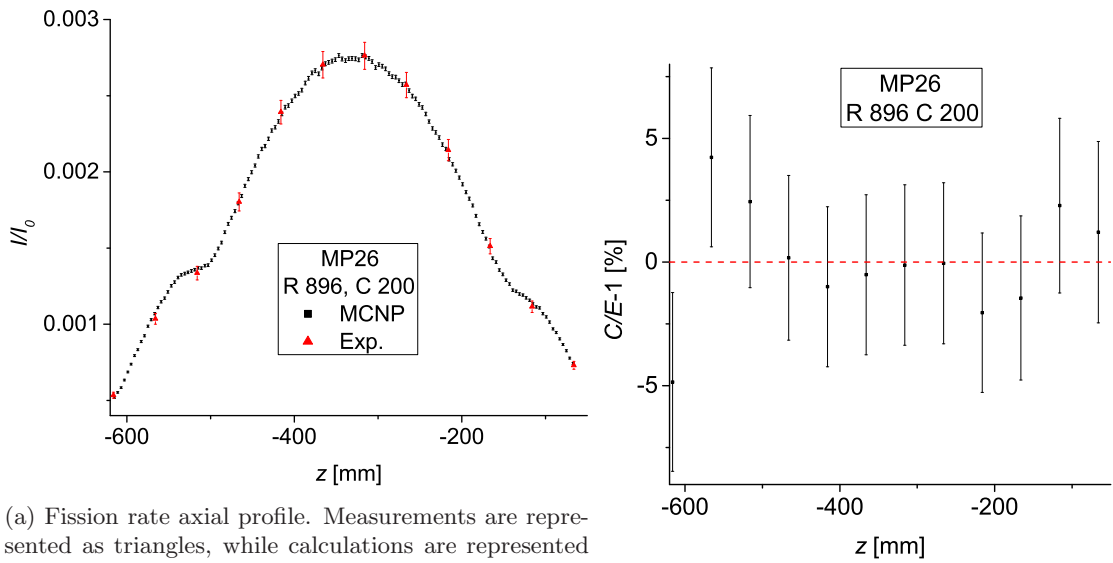
(a) Fission rate axial profile. Measurements are represented as triangles, while calculations are represented as dots. Error bars represent  $1\sigma$  statistical and measurement uncertainties. (b) The deviation between experiment (E) and calculations (C). Error bars present uncertainty that was derived by taking into account  $1\sigma$  statistical and measurement uncertainties.

Figure A.5: Measured and calculated fission rate in MP20 at R CR in position 380. The corresponding calculated  $\chi^2/U = 0.668$ .



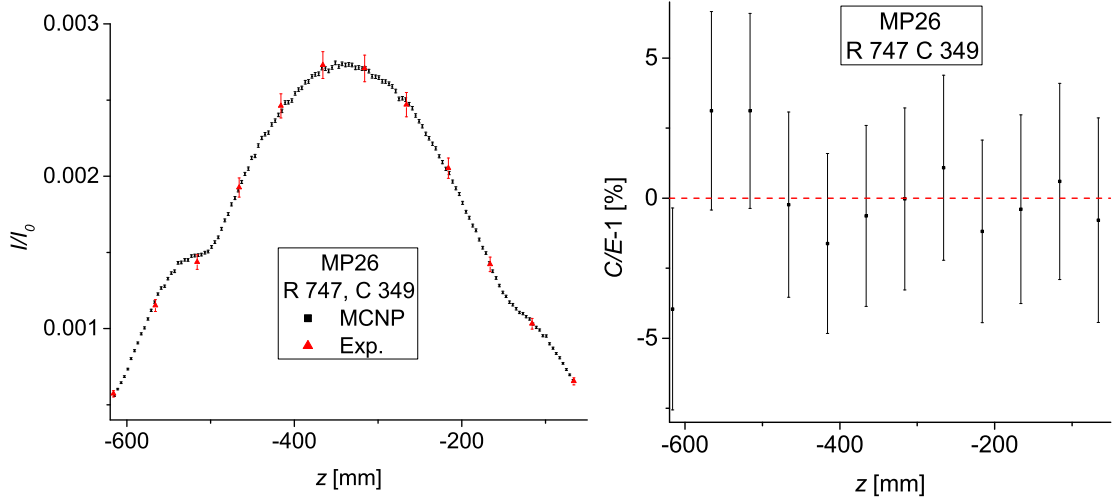
(a) Fission rate axial profile. Measurements are represented as triangles, while calculations are represented as dots. Error bars represent  $1\sigma$  statistical and measurement uncertainties. (b) The deviation between experiment (E) and calculations (C). Error bars present uncertainty that was derived by taking into account  $1\sigma$  statistical and measurement uncertainties.

Figure A.6: Fission rate axial profiles in MP20 at R CR in position 220. The corresponding calculated  $\chi^2/U = 0.803$ .



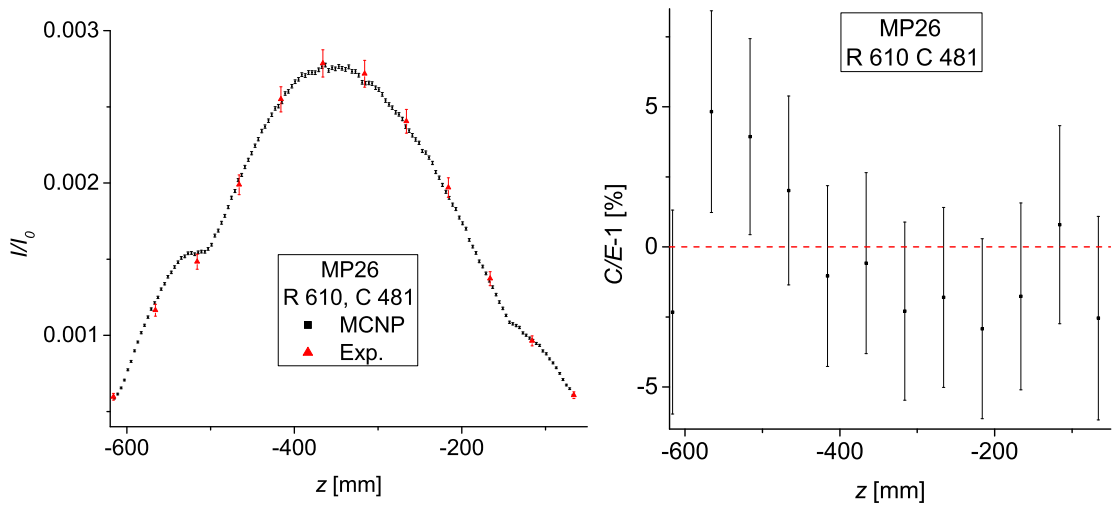
(a) Fission rate axial profile. Measurements are represented as triangles, while calculations are represented as dots. Error bars represent  $1\sigma$  statistical and measurement uncertainties.

Figure A.7: Measured and calculated fission rate in MP26 at R CR in position 896. The corresponding calculated  $\chi^2/U = 0.426$ .



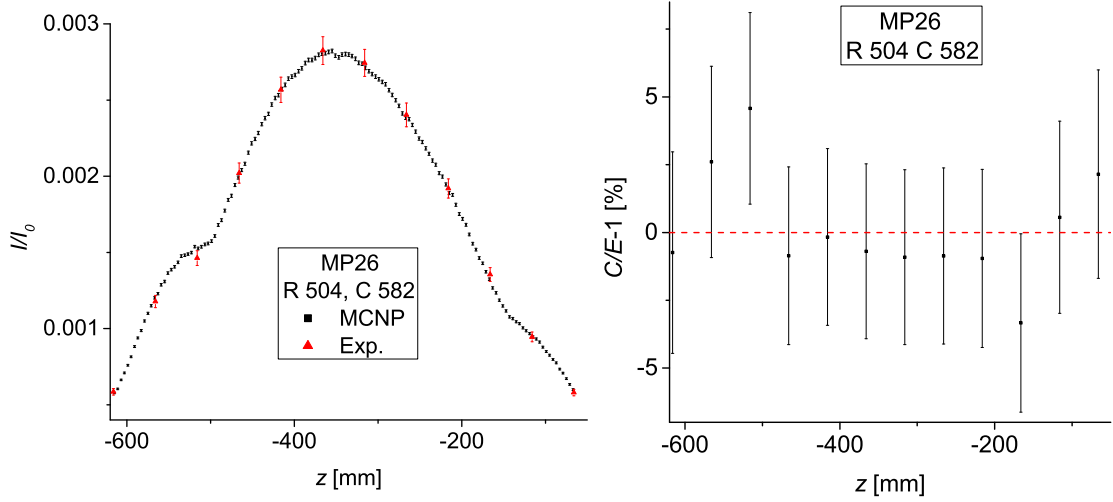
(a) Fission rate axial profile. Measurements are represented as triangles, while calculations are represented as dots. Error bars represent  $1\sigma$  statistical and measurement uncertainties. (b) The deviation between experiment (E) and calculations (C). Error bars present uncertainty that was derived by taking into account  $1\sigma$  statistical and measurement uncertainties.

Figure A.8: Measured and calculated fission rate in MP26 at R CR in position 747. The corresponding calculated  $\chi^2/U = 0.296$ .



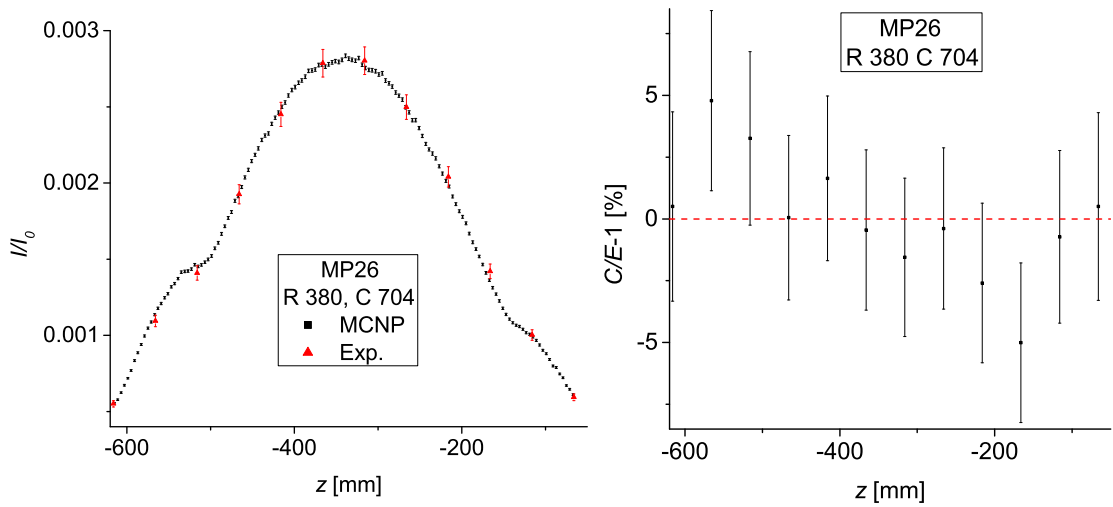
(a) Fission rate axial profile. Measurements are represented as triangles, while calculations are represented as dots. Error bars represent  $1\sigma$  statistical and measurement uncertainties. (b) The deviation between experiment (E) and calculations (C). Error bars present uncertainty that was derived by taking into account  $1\sigma$  statistical and measurement uncertainties.

Figure A.9: Measured and calculated fission rate in MP26 at R CR in position 610. The corresponding calculated  $\chi^2/U = 0.568$ .



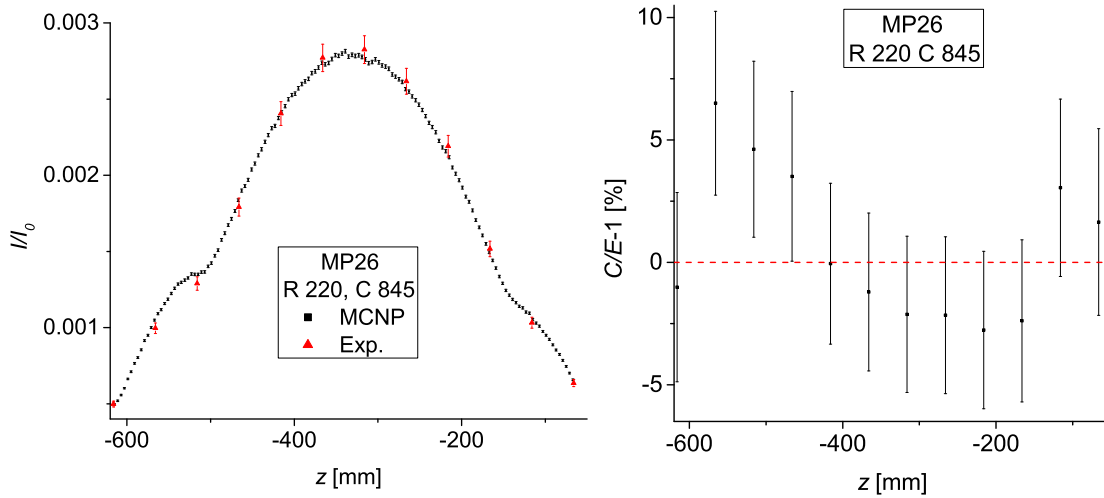
(a) Fission rate axial profile. Measurements are represented as triangles, while calculations are represented as dots. Error bars represent  $1\sigma$  statistical and measurement uncertainties. (b) The deviation between experiment (E) and calculations (C). Error bars present uncertainty that was derived by taking into account  $1\sigma$  statistical and measurement uncertainties.

Figure A.10: Measured and calculated fission rate in MP26 at R CR in position 504. The corresponding calculated  $\chi^2/U = 0.354$ .



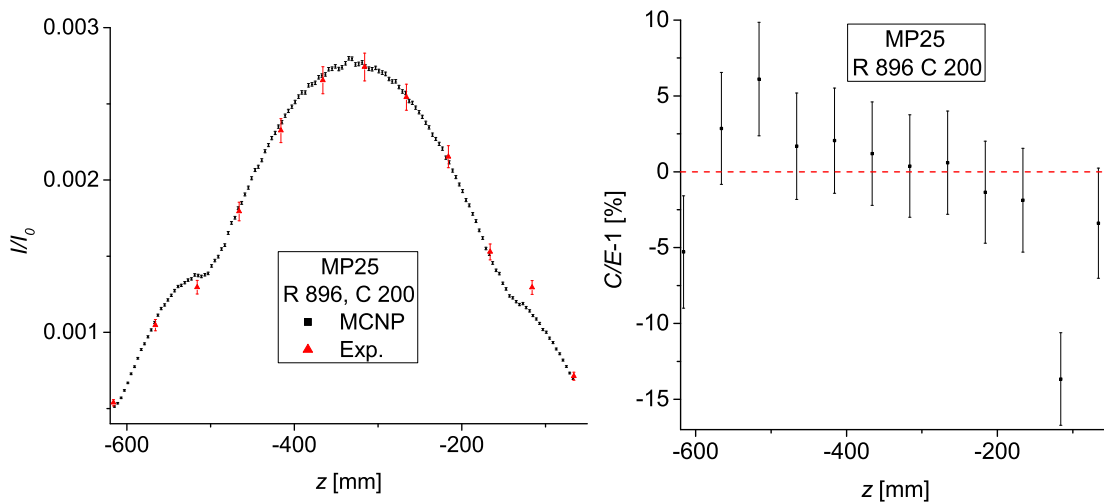
(a) Fission rate axial profile. Measurements are represented as triangles, while calculations are represented as dots. Error bars represent  $1\sigma$  statistical and measurement uncertainties. (b) The deviation between experiment (E) and calculations (C). Error bars present uncertainty that was derived by taking into account  $1\sigma$  statistical and measurement uncertainties.

Figure A.11: Measured and calculated fission rate in MP26 at R CR in position 380. The corresponding calculated  $\chi^2/U = 0.530$ .



(a) Fission rate axial profile. Measurements are represented as triangles, while calculations are represented as dots. Error bars represent  $1\sigma$  statistical and measurement uncertainties. (b) The deviation between experiment (E) and calculations (C). Error bars present uncertainty that was derived by taking into account  $1\sigma$  statistical and measurement uncertainties.

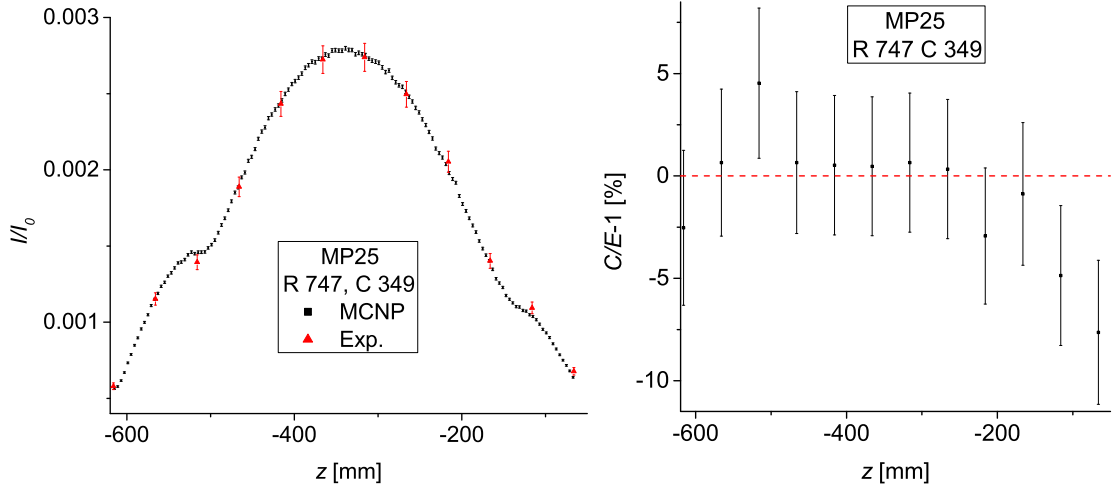
Figure A.12: Measured and calculated fission rate in MP26 at R CR in position 220. The corresponding calculated  $\chi^2/U = 0.817$ .



(a) Fission rate axial profile. Measurements are represented as triangles, while calculations are represented as dots. Error bars represent  $1\sigma$  statistical and measurement uncertainties. (b) The deviation between experiment (E) and calculations (C). Error bars present uncertainty that was derived by taking into account  $1\sigma$  statistical and measurement uncertainties.

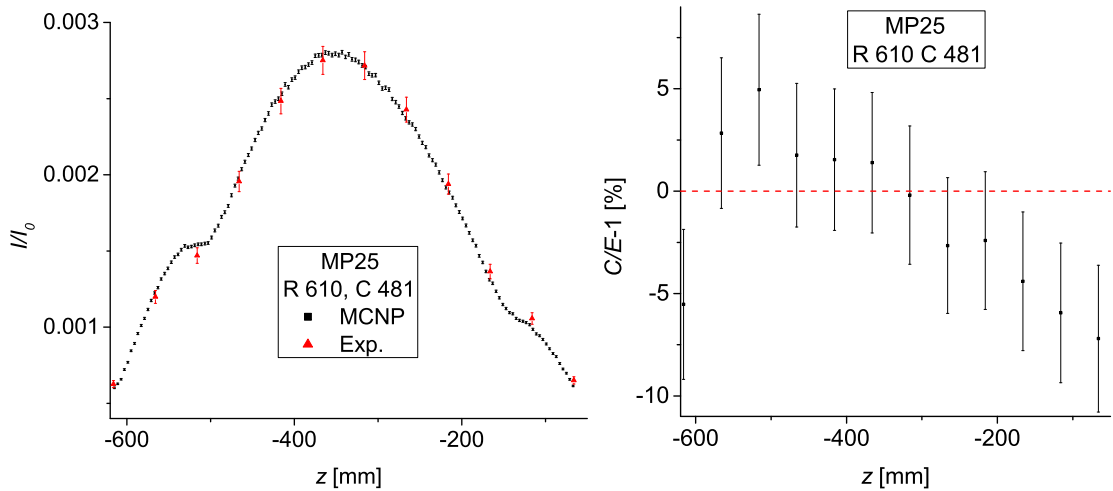
Figure A.13: Measured and calculated fission rate in MP25 at R CR in position 896. The corresponding calculated  $\chi^2/U = 1.938$





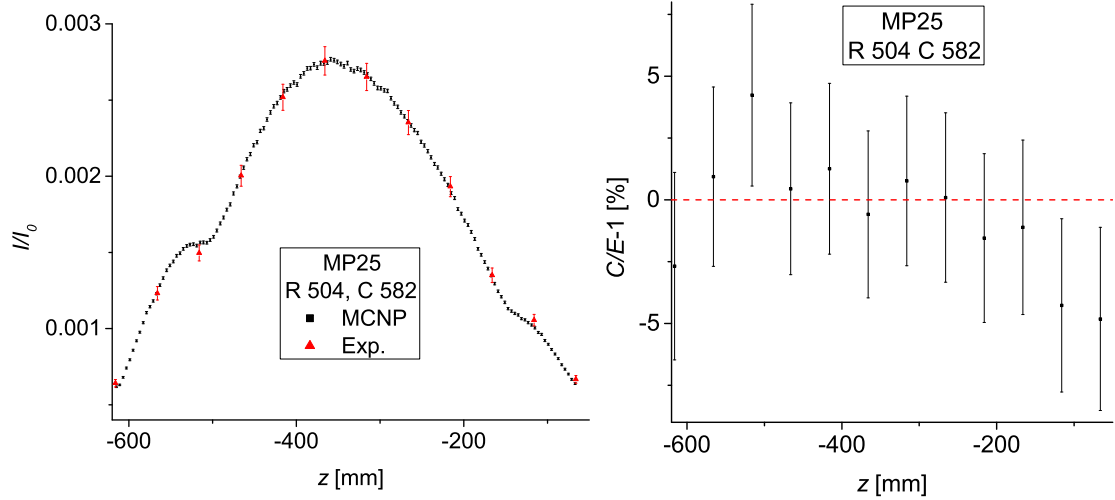
(a) Fission rate axial profile. Measurements are represented as triangles, while calculations are represented as squares. Error bars represent  $1\sigma$  statistical and measurement uncertainties. (b) The deviation between experiment (E) and calculations (C). Error bars present uncertainty that was derived by taking into account  $1\sigma$  statistical and measurement uncertainties.

Figure A.14: Measured and calculated fission rate in MP25 at R CR in position 747. The corresponding calculated  $\chi^2/U = 0.774$ .



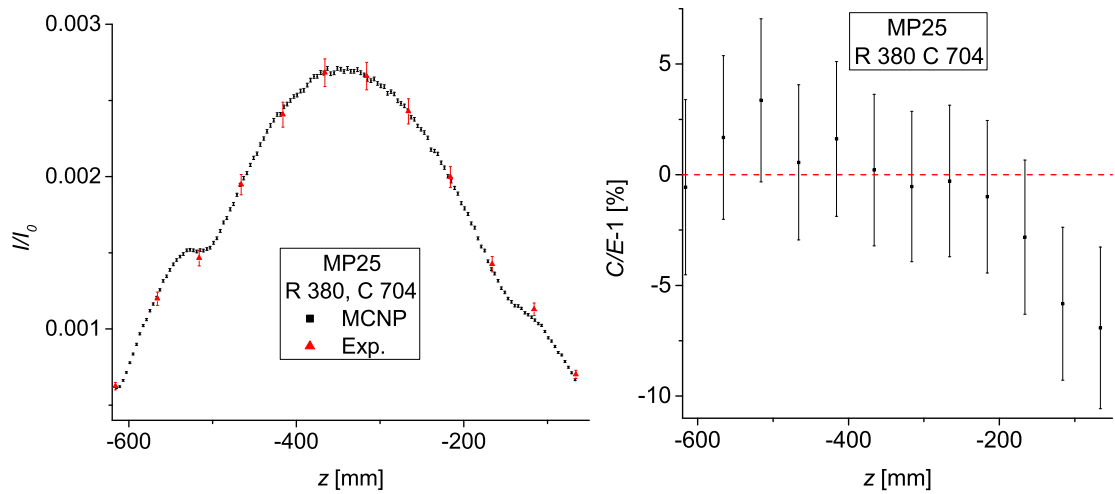
(a) Fission rate axial profile. Measurements are represented as triangles, while calculations are represented as squares. Error bars represent  $1\sigma$  statistical and measurement uncertainties. (b) The deviation between experiment (E) and calculations (C). Error bars present uncertainty that was derived by taking into account  $1\sigma$  statistical and measurement uncertainties.

Figure A.15: Measured and calculated fission rate in MP25 at R CR in position 610. The corresponding calculated  $\chi^2/U = 1.221$ .



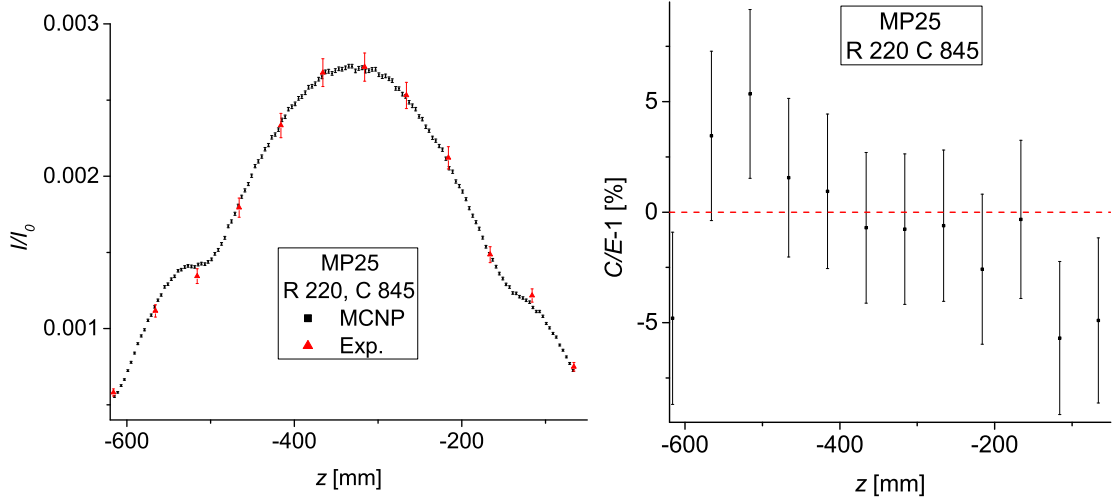
(a) Fission rate axial profile. Measurements are represented as triangles, while calculations are represented as dots. Error bars represent  $1\sigma$  statistical and measurement uncertainties. (b) The deviation between experiment (E) and calculations (C). Error bars present uncertainty that was derived by taking into account  $1\sigma$  statistical and measurement uncertainties.

Figure A.16: Measured and calculated fission rate in MP25 at R CR in position 504. The corresponding calculated  $\chi^2/U = 0.468$ .



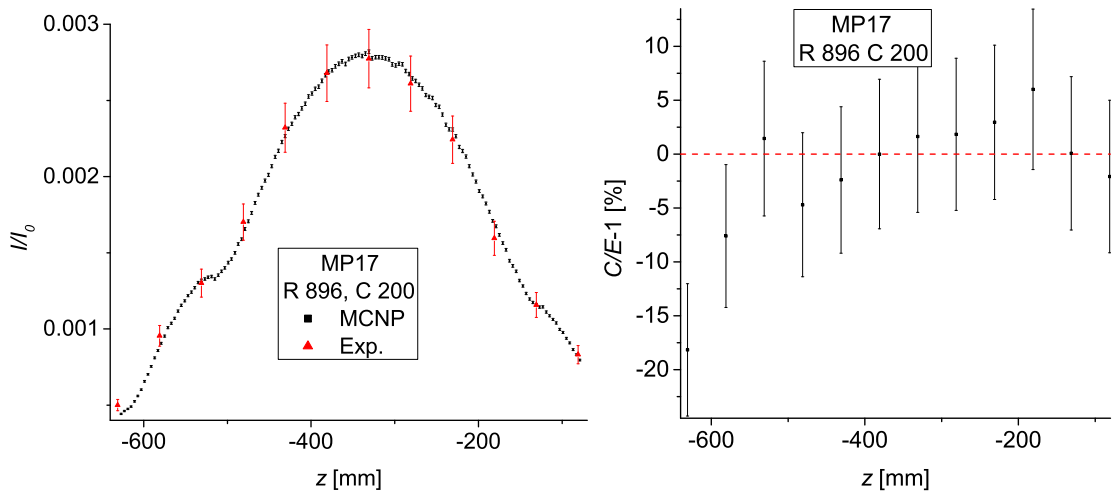
(a) Fission rate axial profile. Measurements are represented as triangles, while calculations are represented as dots. Error bars represent  $1\sigma$  statistical and measurement uncertainties. (b) The deviation between experiment (E) and calculations (C). Error bars present uncertainty that was derived by taking into account  $1\sigma$  statistical and measurement uncertainties.

Figure A.17: Measured and calculated fission rate in MP25 at R CR in position 380. The corresponding calculated  $\chi^2/U = 0.672$ .



(a) Fission rate axial profile. Measurements are represented as triangles, while calculations are represented as dots. Error bars represent  $1\sigma$  statistical and measurement uncertainties. (b) The deviation between experiment (E) and calculations (C). Error bars present uncertainty that was derived by taking into account  $1\sigma$  statistical and measurement uncertainties.

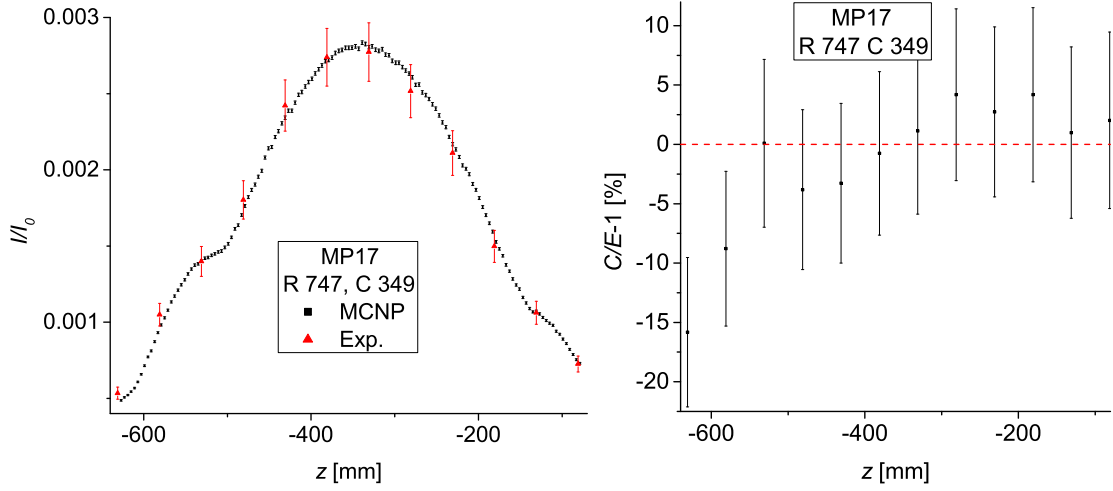
Figure A.18: Measured and calculated fission rate in MP25 at R CR in position 220. The corresponding calculated  $\chi^2/U = 0.807$ .



(a) Fission rate axial profile. Measurements are represented as triangles, while calculations are represented as dots. Error bars represent  $1\sigma$  statistical and measurement uncertainties. (b) The deviation between experiment (E) and calculations (C). Error bars present uncertainty that was derived by taking into account  $1\sigma$  statistical and measurement uncertainties.

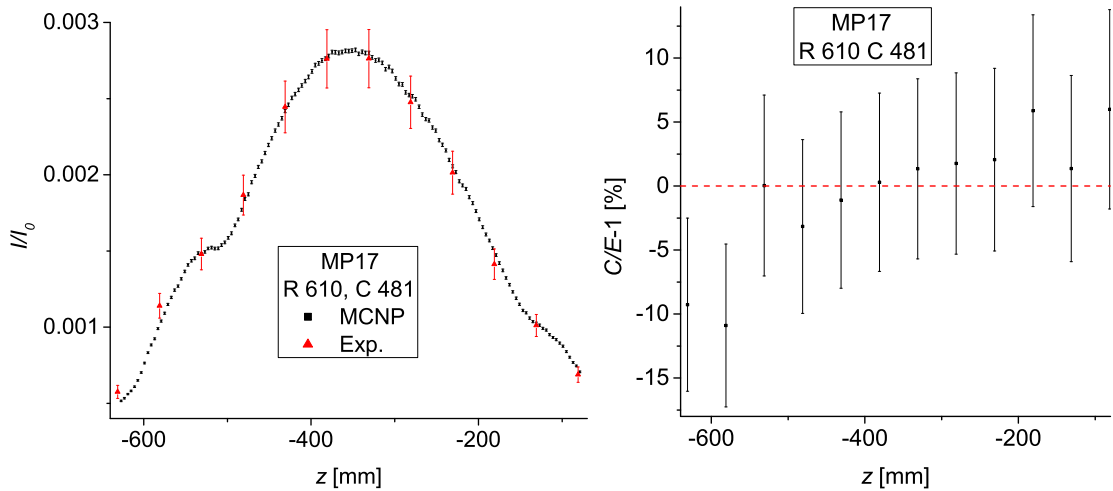
Figure A.19: Measured and calculated fission rate in MP17 at R CR in position 896. The corresponding calculated  $\chi^2/U = 0.737$ .





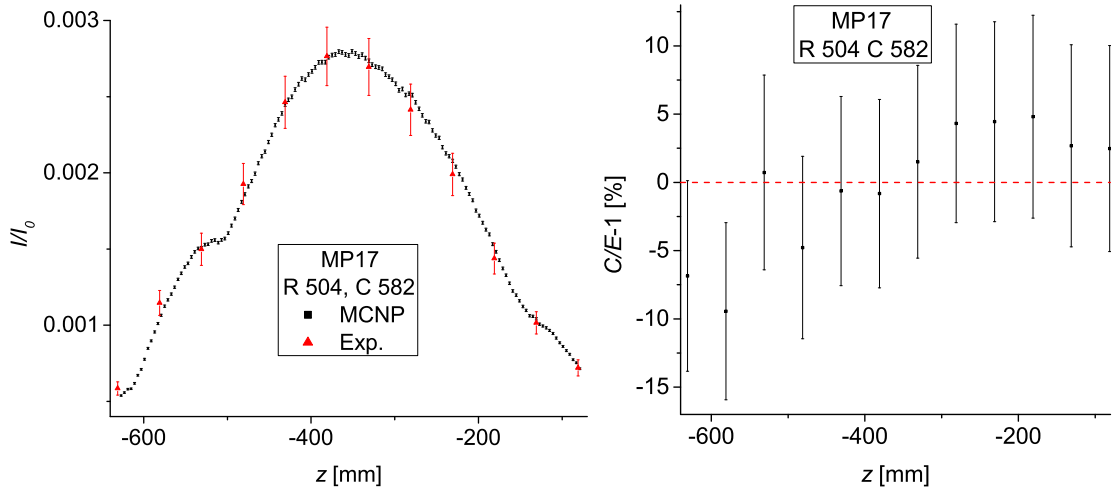
(a) Fission rate axial profile. Measurements are represented as triangles, while calculations are represented as squares. Error bars represent  $1\sigma$  statistical and measurement uncertainties. (b) The deviation between experiment (E) and calculations (C). Error bars present uncertainty that was derived by taking into account  $1\sigma$  statistical and measurement uncertainties.

Figure A.20: Measured and calculated fission rate in MP17 at R CR in position 747. The corresponding calculated  $\chi^2/U = 0.636$ .



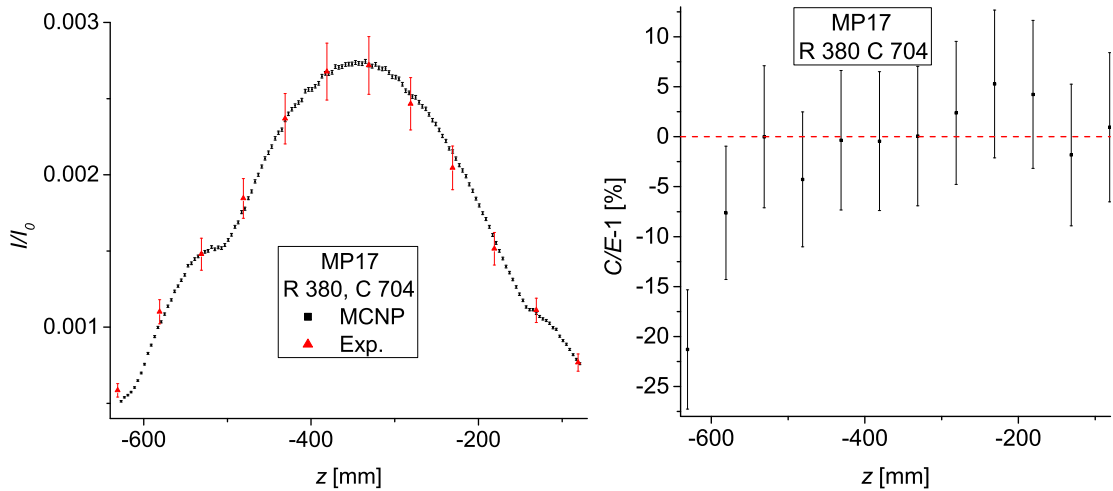
(a) Fission rate axial profile. Measurements are represented as triangles, while calculations are represented as squares. Error bars represent  $1\sigma$  statistical and measurement uncertainties. (b) The deviation between experiment (E) and calculations (C). Error bars present uncertainty that was derived by taking into account  $1\sigma$  statistical and measurement uncertainties.

Figure A.21: Measured and calculated fission rate in MP17 at R CR in position 610. The corresponding calculated  $\chi^2/U = 0.478$ .



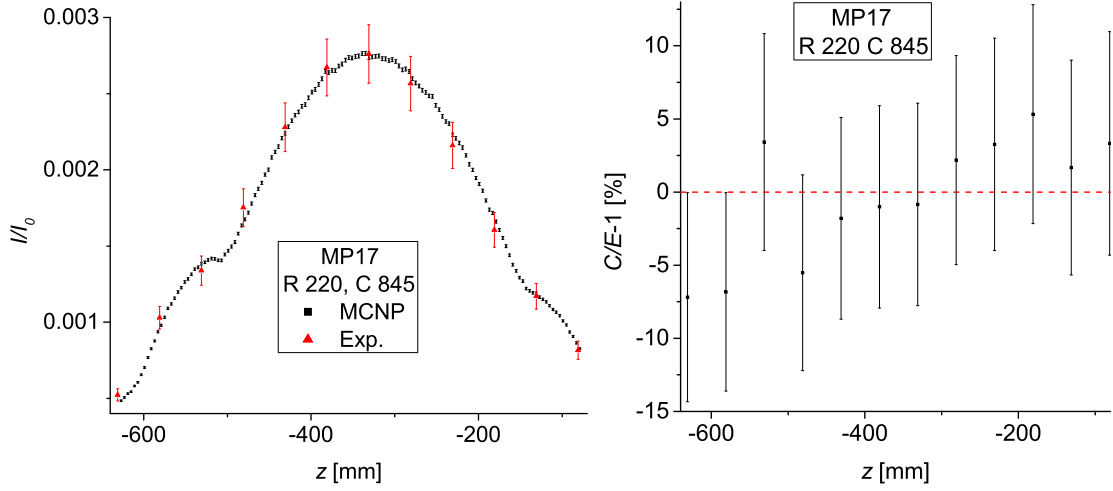
(a) Fission rate axial profile. Measurements are represented as triangles, while calculations are represented as squares. Error bars represent  $1\sigma$  statistical and measurement uncertainties. (b) The deviation between experiment (E) and calculations (C). Error bars present uncertainty that was derived by taking into account  $1\sigma$  statistical and measurement uncertainties.

Figure A.22: Measured and calculated fission rate in MP17 at R CR in position 504. The corresponding calculated  $\chi^2/U = 0.388$ .



(a) Fission rate axial profile. Measurements are represented as triangles, while calculations are represented as squares. Error bars represent  $1\sigma$  statistical and measurement uncertainties. (b) The deviation between experiment (E) and calculations (C). Error bars present uncertainty that was derived by taking into account  $1\sigma$  statistical and measurement uncertainties.

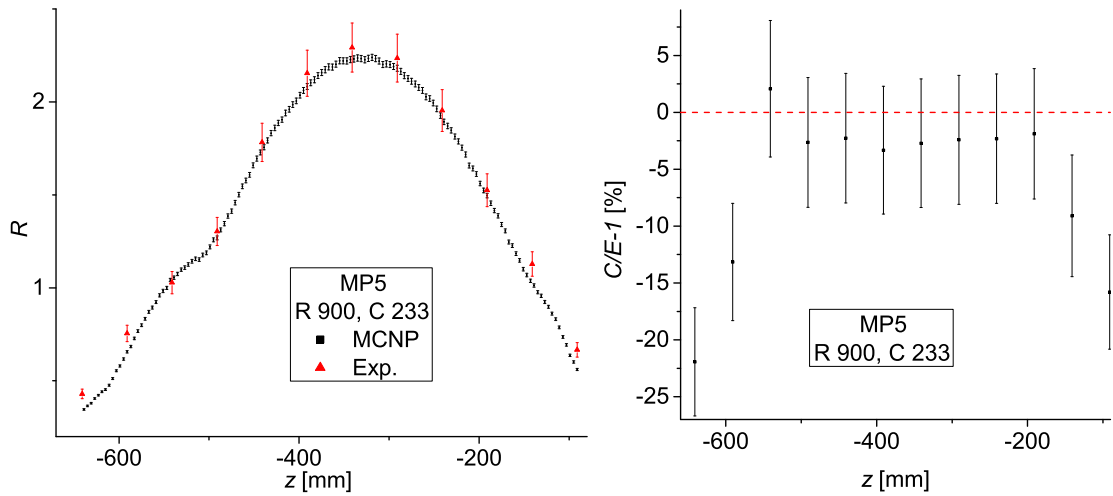
Figure A.23: Measured and calculated fission rate in MP17 at R CR in position 380. The corresponding calculated  $\chi^2/U = 0.888$ .



(a) Fission rate axial profile. Measurements are represented as triangles, while calculations are represented as squares. Error bars represent  $1\sigma$  statistical and measurement uncertainties. (b) The deviation between experiment (E) and calculations (C). Error bars present uncertainty that was derived by taking into account  $1\sigma$  statistical and measurement uncertainties.

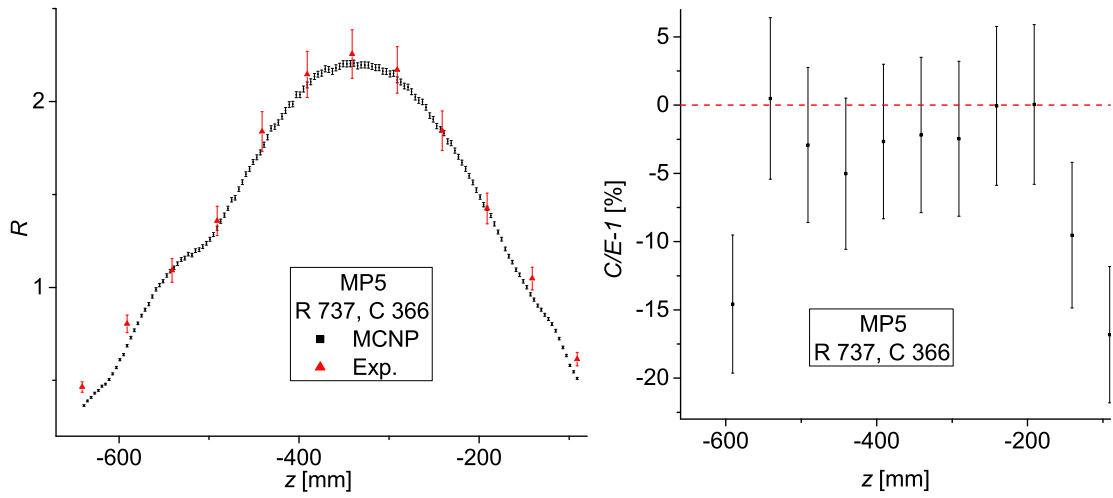
Figure A.24: Measured and calculated fission rate in MP17 at R CR in position 220. The corresponding calculated  $\chi^2/U = 0.321$ .

## A.2 Second set



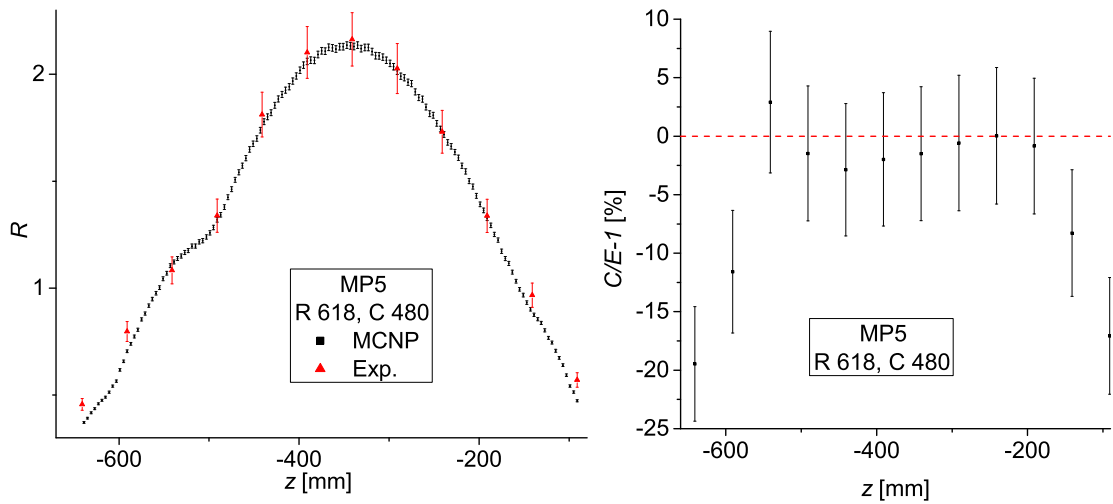
(a) Fission rate axial profile. Measurements are represented as triangles, while calculations are represented as squares. Error bars represent  $1\sigma$  statistical and measurement uncertainties. (b) The deviation between experiment (E) and calculations (C). Error bars present uncertainty that was derived by taking into account  $1\sigma$  statistical and measurement uncertainties.

Figure A.25: Measured and calculated fission rate in MP5 at R CR in position 900. The corresponding calculated  $\chi^2/U = 2.47$ .



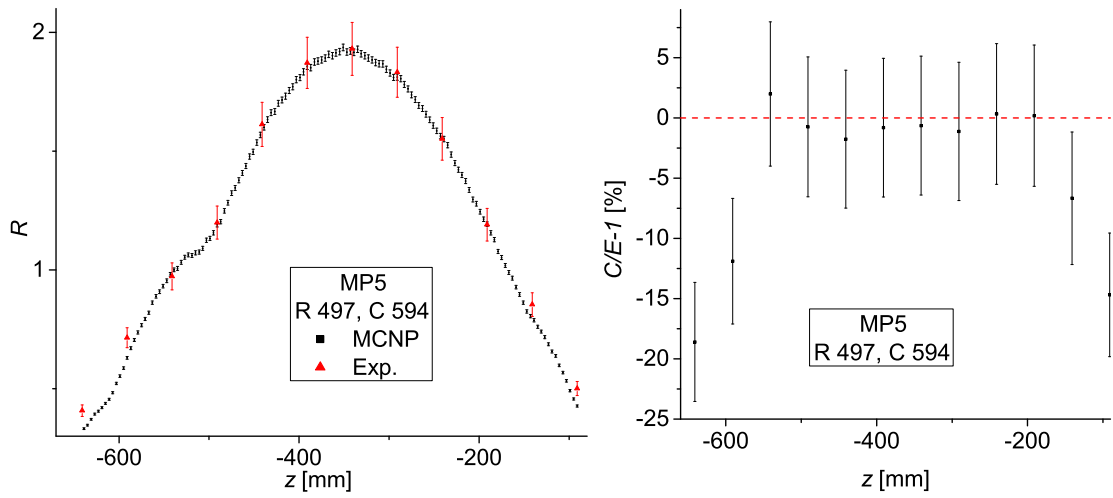
(a) Fission rate axial profile. Measurements are represented as triangles, while calculations are represented as dots. Error bars represent  $1\sigma$  statistical and measurement uncertainties. (b) The deviation between experiment (E) and calculations (C). Error bars present uncertainty that was derived by taking into account  $1\sigma$  statistical and measurement uncertainties.

Figure A.26: Measured and calculated fission rate in MP5 at R CR in position 737. The corresponding calculated  $\chi^2/U = 3.01$ .



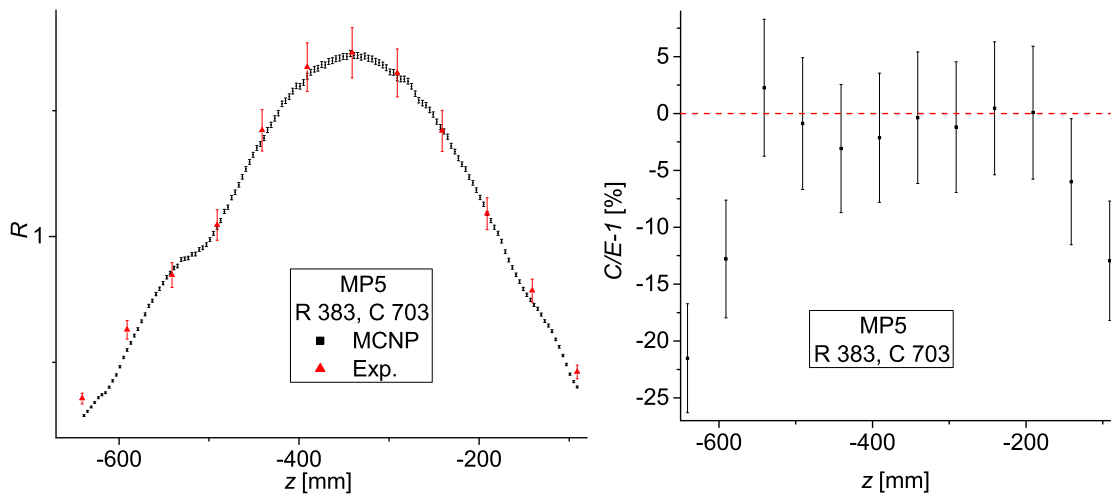
(a) Fission rate axial profile. Measurements are represented as triangles, while calculations are represented as dots. Error bars represent  $1\sigma$  statistical and measurement uncertainties. (b) The deviation between experiment (E) and calculations (C). Error bars present uncertainty that was derived by taking into account  $1\sigma$  statistical and measurement uncertainties.

Figure A.27: Measured and calculated fission rate in MP5 at R CR in position 618. The corresponding calculated  $\chi^2/U = 2.14$ .



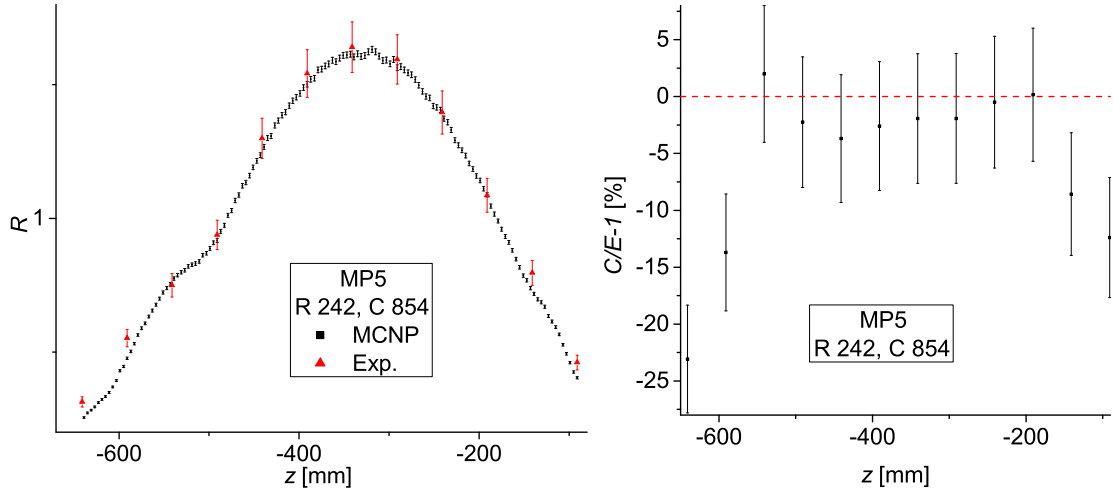
(a) Fission rate axial profile. Measurements are represented as triangles, while calculations are represented as squares. Error bars represent 1 $\sigma$  statistical and measurement uncertainties. (b) The deviation between experiment (E) and calculations (C). Error bars present uncertainty that was derived by taking into account 1 $\sigma$  statistical and measurement uncertainties.

Figure A.28: Measured and calculated fission rate in MP5 at R CR in position 497. The corresponding calculated  $\chi^2/U = 1.80$ .



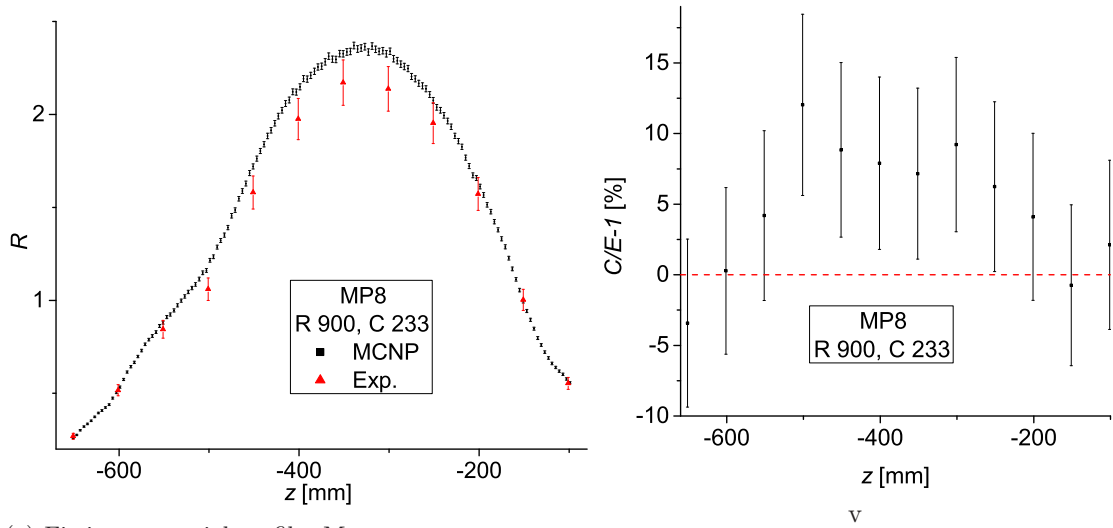
(a) Fission rate axial profile. Measurements are represented as triangles, while calculations are represented as squares. Error bars represent 1 $\sigma$  statistical and measurement uncertainties. (b) The deviation between experiment (E) and calculations (C). Error bars present uncertainty that was derived by taking into account 1 $\sigma$  statistical and measurement uncertainties.

Figure A.29: Measured and calculated fission rate in MP5 at R CR in position 383. The corresponding calculated  $\chi^2/U = 2.01$ .



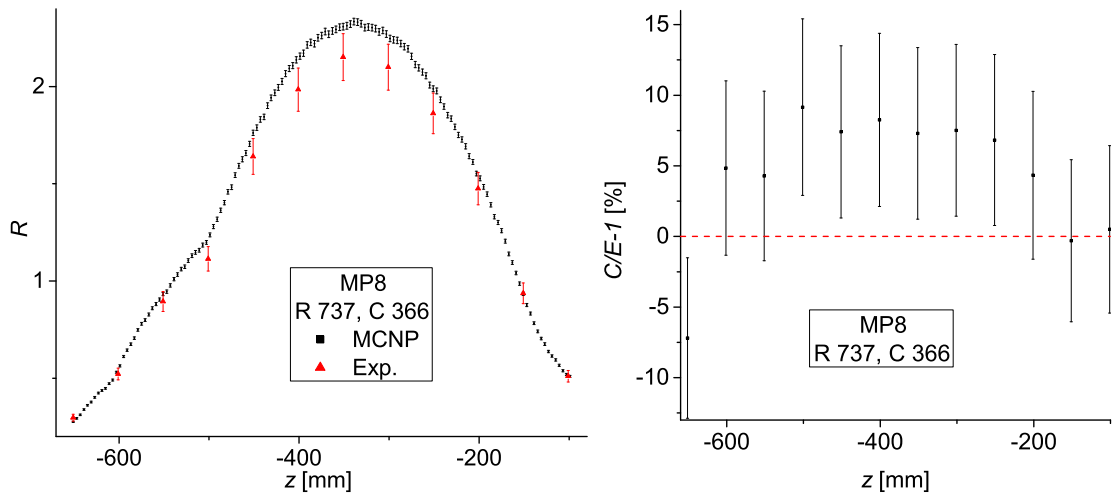
(a) Fission rate axial profile. Measurements are represented as triangles, while calculations are represented as dots. Error bars represent  $1\sigma$  statistical and measurement uncertainties. (b) The deviation between experiment (E) and calculations (C). Error bars present uncertainty that was derived by taking into account  $1\sigma$  statistical and measurement uncertainties.

Figure A.30: Measured and calculated fission rate in MP5 at R CR in position 242. The corresponding calculated  $\chi^2/U = 2.30$ .



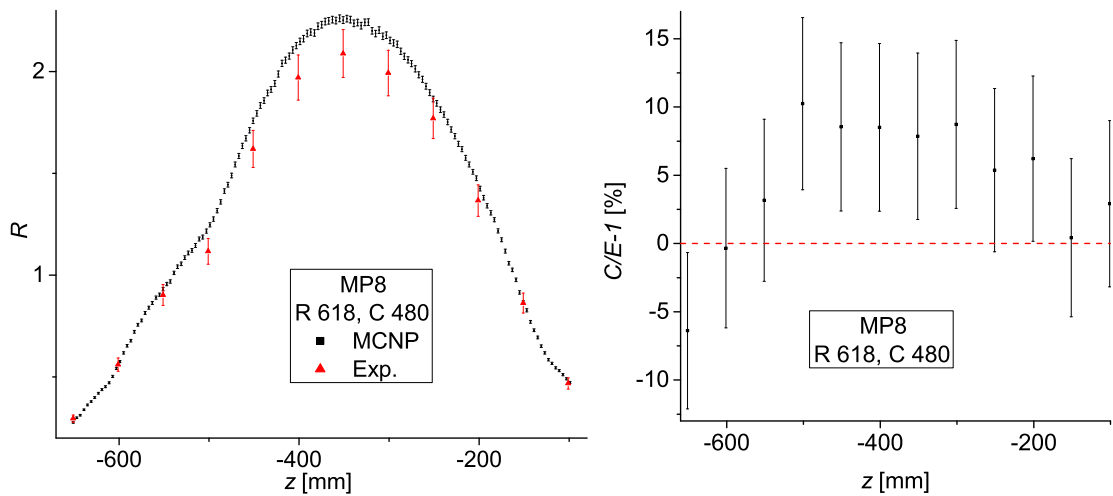
(a) Fission rate axial profile. Measurements are represented as triangles, while calculations are represented as dots. Error bars represent  $1\sigma$  statistical and measurement uncertainties. (b) The deviation between experiment (E) and calculations (C). Error bars present uncertainty that was derived by taking into account  $1\sigma$  statistical and measurement uncertainties.

Figure A.31: Measured and calculated fission rate in MP8 at R CR in position 900. The corresponding calculated  $\chi^2/U = 1.34$ .



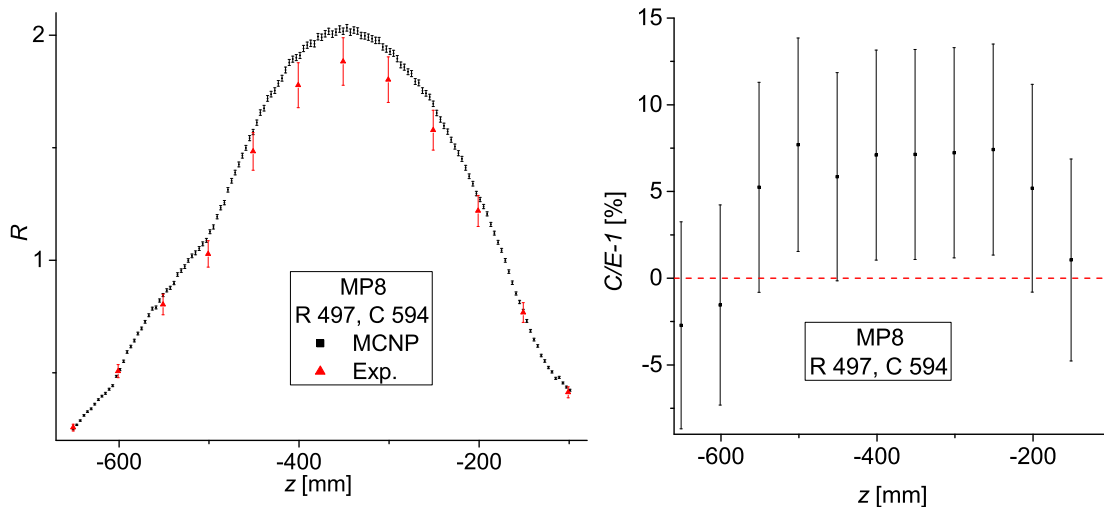
(a) Fission rate axial profile. Measurements are represented as triangles, while calculations are represented as squares. Error bars represent  $1\sigma$  statistical and measurement uncertainties. (b) The deviation between experiment (E) and calculations (C). Error bars present uncertainty that was derived by taking into account  $1\sigma$  statistical and measurement uncertainties.

Figure A.32: Measured and calculated fission rate in MP8 at R CR in position 737. The corresponding calculated  $\chi^2/U = 1.23$ .



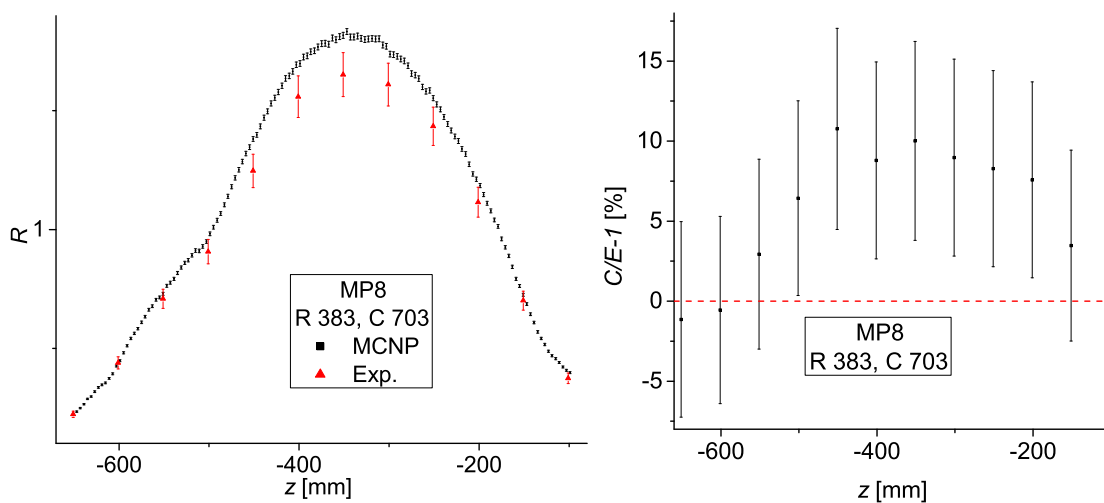
(a) Fission rate axial profile. Measurements are represented as triangles, while calculations are represented as squares. Error bars represent  $1\sigma$  statistical and measurement uncertainties. (b) The deviation between experiment (E) and calculations (C). Error bars present uncertainty that was derived by taking into account  $1\sigma$  statistical and measurement uncertainties.

Figure A.33: Measured and calculated fission rate in MP8 at R CR in position 618. The corresponding calculated  $\chi^2/U = 1.34$ .



(a) Fission rate axial profile. Measurements are represented as triangles, while calculations are represented as dots. Error bars represent  $1\sigma$  statistical and measurement uncertainties. (b) The deviation between experiment (E) and calculations (C). Error bars present uncertainty that was derived by taking into account  $1\sigma$  statistical and measurement uncertainties.

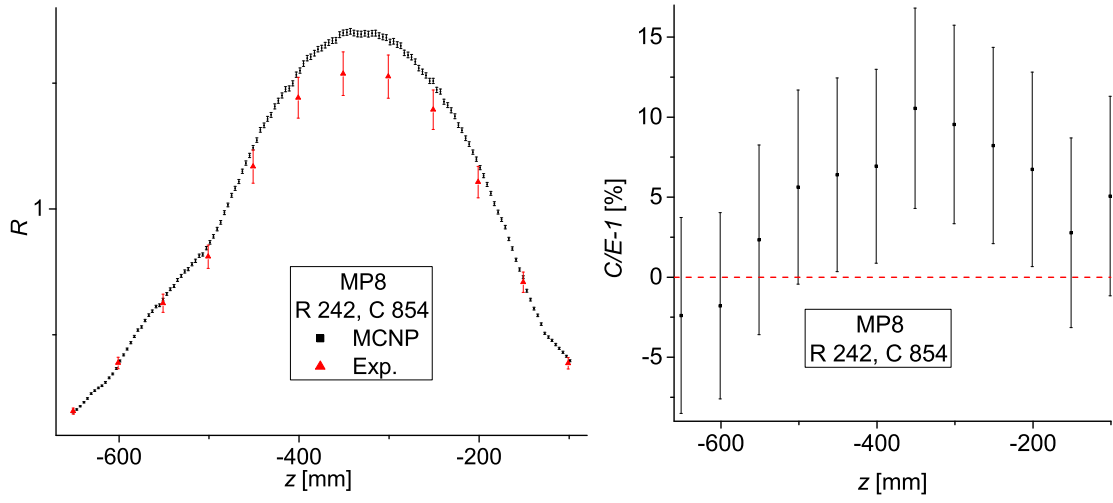
Figure A.34: Measured and calculated fission rate in MP8 at R CR in position 900. The corresponding calculated  $\chi^2/U = 1.00$ .



(a) Fission rate axial profile. Measurements are represented as triangles, while calculations are represented as dots. Error bars represent  $1\sigma$  statistical and measurement uncertainties. (b) The deviation between experiment (E) and calculations (C). Error bars present uncertainty that was derived by taking into account  $1\sigma$  statistical and measurement uncertainties.

Figure A.35: Measured and calculated fission rate in MP8 at R CR in position 383. The corresponding calculated  $\chi^2/U = 1.62$ .





(a) Fission rate axial profile. Measurements are represented as triangles, while calculations are represented as dots. Error bars represent  $1\sigma$  statistical and measurement uncertainties. (b) The deviation between experiment (E) and calculations (C). Error bars present uncertainty that was derived by taking into account  $1\sigma$  statistical and measurement uncertainties.

Figure A.36: Measured and calculated fission rate in MP8 at R CR in position 242. The corresponding calculated  $\chi^2/U = 1.26$ .